ACS NANO MEDICINE

Editors' Choice

pubs.acs.org/ACSNanoMed

Article

Vascular-Protective Effects of Cerium Oxide Nanoparticles Complexed with Iron Oxide and Methotrexate: Reversing Atherosclerosis in a Murine Model

Yuao Wu, Huong D. N. Tran, Dimple Sajin, Shehzahdi S. Moonshi, Najma Annuria Fithri, Nyoman Kurniawan, and Hang Thu Ta*

Cite This: *ACS Nano Med.* 2026, 1, 250−267

Read Online

ACCESS | Metrics & More | Article Recommendations | Supporting Information

ABSTRACT: Atherosclerosis is a leading cause of cardiovascular morbidity, characterized by chronic inflammation and excessive production of reactive oxygen species (ROS). Despite advances in therapy, effective diagnostic and therapeutic strategies that can both visualize and modulate vascular inflammation remain limited. Here, we designed a chitosan-stabilized cerium oxide−iron oxide nanocomplex conjugated with methotrexate and Cy5 (Chit-IOCO-Cy5-MTX) to achieve simultaneous ROS scavenging, anti-inflammatory activity, and magnetic resonance imaging (MRI). The nanocomplex exhibited strong T_2 relaxivity (r_2 = 281 mM^{-1} s^{-1}) and high colloidal stability. In vitro, Chit-IOCO-Cy5-MTX was efficiently internalized by LPS-activated RAW 264.7 macrophages, markedly reducing intracellular ROS levels and suppressing pro-inflammatory cytokines (IL-6, TNF-α, COX-2). In ApoE$^{-/-}$ mice, MRI and ex vivo fluorescence confirmed targeted accumulation in atherosclerotic plaques. Four-week treatment significantly decreased plaque area and inflammatory protein expression compared to saline and non-MTX controls, without detectable systemic toxicity. Overall, this study demonstrates a cerium oxide−iron oxide nanotheranostic platform that enables targeted imaging and effective modulation of oxidative and inflammatory pathways in atherosclerosis, highlighting its translational potential for vascular inflammatory diseases.

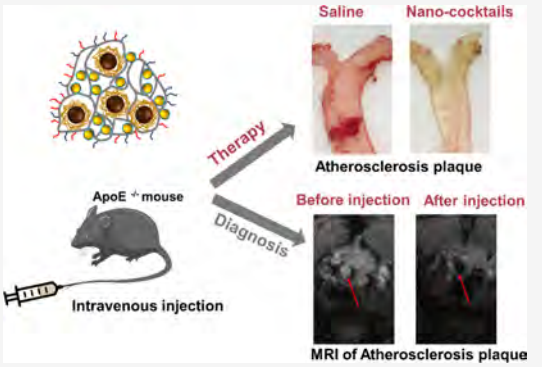

KEYWORDS: *atherosclerosis, molecular imaging, theranostics, iron oxide, cerium oxide, chitosan*

INTRODUCTION

Atherosclerosis is a multifaceted disorder that affects the inner layer of arteries and can develop gradually over several years.[1,2] Rupture of vulnerable atherosclerotic plaques results in thrombosis, which can lead to heart attack and stroke.[3,4] Inflammation has been established as a critical factor in all phases of atherosclerosis, from its initiation to progression and the development of thrombotic complications.[5,6] Reactive oxygen species (ROS) is also a key contributor to the progression of atherosclerosis, by promoting the production of oxidized low density lipoproteins in blood vessels.[7] Additionally, ROS can stimulate the secretion of growth factors such as interleukin 6 (IL-6) and tumor necrosis factor-α (TNF-α), further worsening the condition.[8] Besides, the overproduction of free radical nitric oxide, which is mediated by the inducible nitric oxide synthase (iNOS), plays a critical role in inflammatory diseases through its heightened activity in macrophages upon cytokine stimulation. Furthermore, cyclooxygenase-2 (COX-2) expression, especially when coupled with proinflammatory microsomal prostaglandin E synthase-1, is proposed as a crucial enzyme in the development of unstable carotid atherosclerotic plaque in several studies.[9]

Recently, there has been a rising interest in exploring the potential benefits of ROS scavenging (anti-ROS) and reduction of inflammation levels in the management of atherosclerosis.[10,11] A number of studies have suggested that such treatments may have positive effects in mitigating the progression of the disease. Recently, cerium oxide nanoparticles have shown regenerative anti-ROS and anti-inflammatory abilities due to their surface valence with both Ce^{3+} and Ce^{4+} atoms present.[12] These nanoparticles have been found to reduce the expression of inflammation-related cytokines and protect against inflammatory diseases.[13−16] Previous works have demonstrated that cerium oxide nanoparticles can reduce plaque progression in vivo.[17] However, these studies mainly focused on intracellular ROS levels or in vitro inflammatory assays, without a detailed evaluation of

Received: July 15, 2025
Revised: October 10, 2025
Accepted: October 20, 2025
Published: November 3, 2025

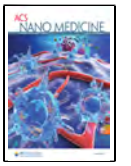

https://doi.org/10.1021/acsnanomed.5c00036
ACS Nano Med. 2026, 1, 250−267

Scheme 1. Illustration of Chitosan Nanocomplexes Synthesis: *In Vitro* and *In Vivo* Investigation

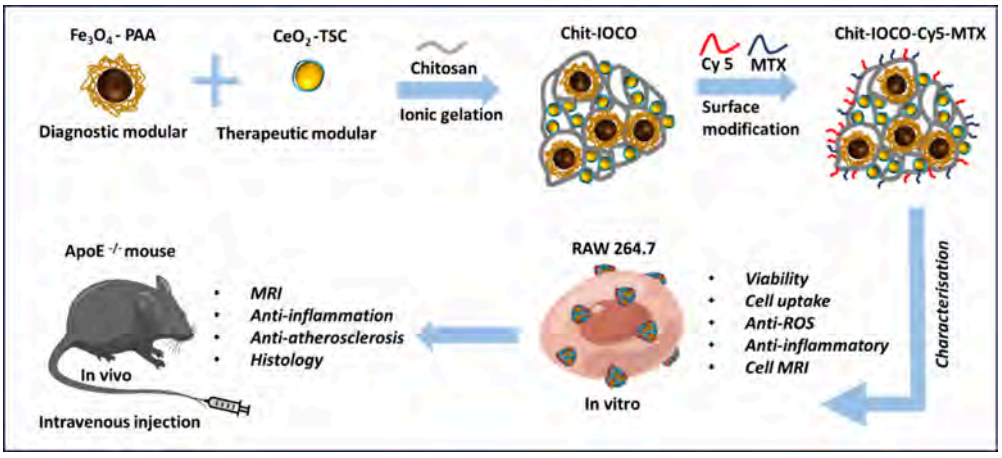

inflammatory responses within atherosclerotic plaques. Despite the widespread use of statins in clinical management of atherosclerosis, their effects are primarily lipid-lowering, and their ability to reduce inflammation and atherosclerotic plaques is dose-dependent, which often requiring high doses that carry risks of hepatotoxicity and myopathy.[18,19] As inflammation and oxidative stress are key drivers of plaque progression and rupture, there is a pressing need for therapeutic strategies that can address both aspects simultaneously.

In this study, we present a targeted theranostic nanoplatform that integrates both therapeutic and diagnostic capabilities into a single system. By harnessing the reactive oxygen species (ROS)-scavenging and anti-inflammatory properties of cerium oxide (CO), along with the site-specific targeting ability of methotrexate (MTX) toward activated macrophages, our nanocomplex provides a dual-action, highly specific strategy for treating atherosclerosis. To enable noninvasive tracking via magnetic resonance imaging (MRI), CO was complexed with iron oxide (IO) using chitosan (Chit) as a stabilizing matrix through an electrostatic self-assembly method, yielding the Chit-IOCO nanocomplex. MRI is among the most widely employed imaging techniques,[20−23] and superparamagnetic iron oxide nanoparticles have been successfully used as contrast agents in the diagnosis of various diseases, including atherosclerosis.[24−26] Electrostatic self-assembly was selected for its simplicity, cost-effectiveness, and ability to avoid the use of complex equipment and hazardous chemicals. This method also offers excellent scalability and reproducibility, making it highly suitable for commercial translation and clinical application.

Recently, we showed that this nanocomplex provides long-lasting anticancer theranostic capabilities.[27] Building on this work, we now take a step further to evaluate the cardiovascular-protective effects of Chit-IOCO and demonstrate its ability to reverse atherosclerosis. This is a significant discovery, as conventional anticancer drugs often pose a risk of cardiotoxicity, whereas Chit-IOCO not only avoids this risk but actively protects the cardiovascular system.

To target CO to atherosclerotic lesions, Chit-IOCO nanocomplexes were labeled with methotrexate (MTX) via a carbodiimide cross-linking reaction. Fluorescence dye Cy-5 was also conjugated onto the nanocomplexes to allow optical imaging. MTX originally developed as an anticancer drug, is now frequently used to treat rheumatoid arthritis and many other chronic inflammatory diseases.[28] MTX achieves its anti-inflammatory effects by inhibiting the synthesis of pyrimidine and purine, and also through the inhibition of polyamine and the release of adenosine.[29] Both rheumatoid arthritis and atherosclerosis are inflammatory diseases that are associated with macrophage dysfunction and cytokines like TNFα, IL-1, and IL-6.[30] Studies have found that MTX can alleviate the symptoms of atherosclerosis in rheumatoid arthritis patients, and it can significantly suppress atherogenesis and related gene expression in cholesterol-fed rabbits.[31] Nonetheless, research conducted by Ridker et al. demonstrated that low-dose methotrexate did not significantly lower the levels of interleukin-1β, interleukin-6, or C-reactive protein, nor did it lead to a reduction in cardiovascular events compared to a placebo in patients with stable atherosclerosis.[32] Consequently, the employment of nanocarriers is imperative to improve the precision of drug delivery, enabling the administration of reduced doses while maintaining comparable therapeutic efficacy. Additionally, MTX which is a competitive antagonist of folic acid, exhibits promise as a targeting ligand for inflammation-associated diseases, due to the abundant over-expression of folate receptors on cells located at inflammatory sites.[33,34] MTX has been shown to bind folate receptors (FRs), particularly FR-β, which is selectively expressed on activated macrophages, as demonstrated in rheumatoid arthritis (RA) synovial macrophages. FR-β expression increases upon activation of monocyte/macrophage cells, making it a potential mechanism for macrophage or inflammation targeting. Moreover, MTX uptake via FR-β has been shown to be inhibited by excess folic acid, supporting its receptor-mediated uptake.[35] Moreover, Methotrexate (MTX) has been demonstrated as an effective targeting ligand for nanoparticles, enhancing cellular uptake through receptor-mediated mechanisms. In a study utilizing MTX-functionalized hyaluronic acid nanoparticles (MTX−HA−OCA/CUR), MTX targeted folate receptors, significantly increasing nanoparticle internalization and therapeutic efficacy in HeLa cells and tumor-bearing mice, compared to nontargeted systems.[36] Similarly, pH-sensitive DSPE-PEG-Imine-MTX nanoparticles encapsulating curcumin (MTX-Imine-M-CUR) showed selective uptake via folate receptor-mediated endocytosis, coupled with efficient intracellular drug release under acidic conditions, leading to superior anticancer activity in vitro and in vivo.[37] Therefore, MTX was employed not only as a synergistic anti-inflammtory agent (in addition to cerium oxide) but also as a targeting ligand, a "one shot for double targets" approach.

https://doi.org/10.1021/acsnanomed.5c00036
ACS Nano Med. 2026, 1, 250−267

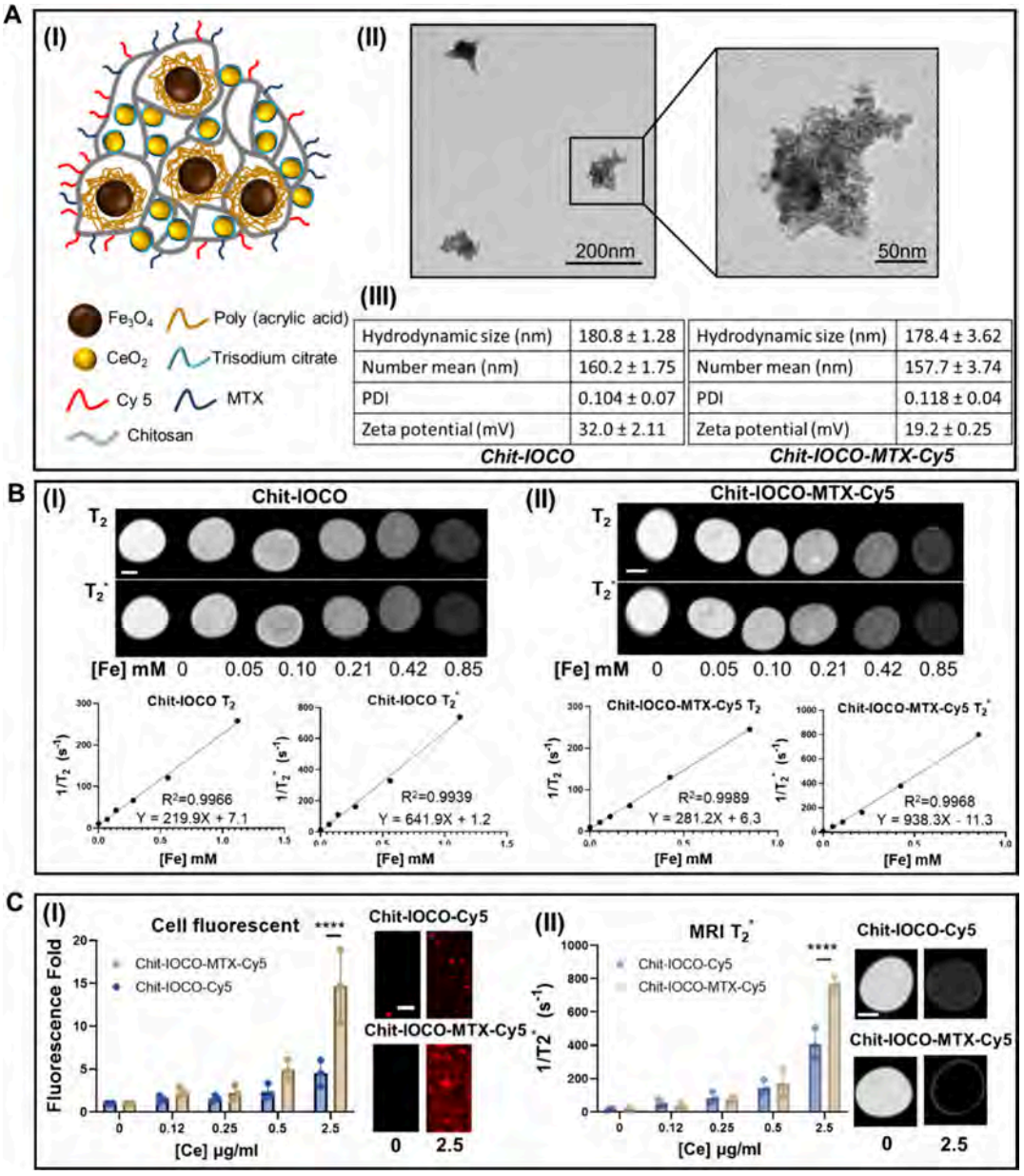

Figure 1. Characterization of nanocomplexes. (A) Structure, size and ZP of Chit-IOCO-Cy5-MTX. (I) A visual representation of the structural of Chit-IOCO-Cy5-MTX. (II) TEM images of Chit-IOCO-Cy5-MTX. (III) Hydrodynamic size, number size, ZP, and PDI of Chit-IOCO and Chit-IOCI-Cy5-MTX. (B) MRI of Chit-IOCO and Chit-IOCO-Cy5-MTX phantoms. The nanocomplexes underwent dilutions to different iron concentrations and then imaged at 9.4 T, T_2 (TE = 5 ms, TR = 2630 ms), T_2* (TE = 3 ms, TR = 300 ms). MRI T_2- and T_2*-weighted images and the plotting of relaxation rate of (I) Chit-IOCO and (II) Chit-IOCO-Cy5-MTX. Bar = 1 mm. (C) *In vitro* targeting ability of nanocomplexes in RAW 264.7. (I) Fluorescence intensity and images of RAW 264.7 cells incubated with or without Chit-IOCO-Cy5 or Chit-IOCO-Cy5-MTX different concentrations of Ce. (II) T_2-weighted MRI signal and images of RAW 264.7 cells incubated with or without Chit-IOCO-Cy5 or Chit-IOCO-Cy5-MTX different concentrations of Ce. Bar = 1 mm. Statistical significance was tested by one-way ANOVA. Mean ± S.D. *Chit-IOCO-Cy5-MTX vs Chit-IOCO-Cy5: ****$p < 0.0001$, $n = 3$.

The resultant nanocomplex (Chit-IOCO-Cy5 and Chit-IOCO-Cy5-MTX) was then subjected to *in vitro* and *in vivo* studies to assess its potential in treating and diagnosing atherosclerosis (Scheme 1). The analysis included evaluation of its biosafety, anti-ROS and anti-inflammatory properties, and ability to provide MRI signal.

■ MATERIALS AND METHODS

Detailed materials and methods are in Supporting Information.

Synthesis of Nanocomplexes

Synthesis of Iron Oxide Nanoparticles and Cerium Oxide Nanoparticles. Poly(acrylic acid) coated iron oxide (IO-PAA) nanoparticles were generated using a coprecipitation approach.[38] Cerium oxide nanoparticles were generated using the precipitation technique.[38]

Synthesis of Chit-IOCO Nanocomplexes. The ionic gelation technique was utilized to fabricate Chit-IOCO nanoparticles, wherein IO-PAA and CO-TSC functioned as cross-linkers.

Synthesis of Chit-IOCO-Cy5 and Chit-IOCO-Cy5-MTX Nanocomplexes. To conjugate MTX and Cy5 dye to the chitosan nanoparticles, an EDC-mediated reaction was deployed to facilitate

https://doi.org/10.1021/acsnanomed.5c00036
ACS Nano Med. 2026, 1, 250−267

amide bond formation between the amino groups of chitosan ($-NH_2$) and the carboxyl groups (−COOH) of either methotrexate (MTX) or Cy5-COOH. EDC was instrumental in activating the −COOH functional groups for this process.

In Vitro ROS Assay

RAW 264.7 cells were cultured in a 96-well plate at 10,000 cells per well for 24 h. These cells were then subjected to LPS treatment with either Chit-IOCO-Cy5 or Chit-IOCO-Cy5-MTX. After 24 h, cells were then treated with 25 μM DCF-DA for 10 min in a 37 °C and 5% CO_2. DCF-DA was used to detect ROS level.

In Vitro Inflammation Assay

RAW 264.7 cells were cultured in a 6-well plate at a seeding density of 200,000 cells per well for a duration of 24 h. The cells then underwent treatment with either cell culture medium (control), 1 μg/mL of LPS (stimulation), or 1 μg/mL of LPS combined with different nanomaterials or MTX at various concentrations (treatment) for another 24 h. Following the treatment, the cells were collected for Western Blotting analysis to evaluate levels of IL-6, TNF-α, COX-2, and iNOS.

Animal Studies

The animal experiment was conducted at the University of Queensland, Brisbane, Australia, following the protocols evaluated and approved by the University of Queensland's animal ethics committee (approval number: AIBN/CAI/133/20). 8-week-old male $ApoE^{-/-}$ and C57BL/6 mice (Animal Resources Centre, Western Australia) were put on a high-fat diet for a period ranging between 7 to 9 weeks. As a control, 8-week-old C57BL/6 mice were kept on a normal diet.

In Vivo MRI

Before contrast agent injection, preinjection MRI scans were performed to obtain a baseline. The mice were anesthetized using 2% isoflurane (Forane), with continuous monitoring of their body temperature (rectal thermometry), respiratory rate (acoustic sensor) and heart rate (pulse oximetry) to ensure their well-being. A heating mat was also employed to maintain a stable body temperature throughout the MRI scanning process. The total duration of the MRI scans was kept to about one hour, optimizing both efficiency and animal comfort. Subsequently, saline, Chit-IOCO-Cy5, and Chit-IOCO-Cy5-MTX were intravenously injected as a single dose after 9 weeks of high fat diet treatment. The postinjection MRI scans were performed 1 day after injection. The conditions for the postinjection scan mirrored those of the preinjection scan to maintain consistency in the procedure. After MRI, the animals were humanely euthanized using cervical dislocation while under anesthetized with 2% isoflurane (Forane) administered via inhalation, ensuring minimal distress to the animals. Their aortas were collected for fluorescence intensity evaluation, and other organs such as the liver, spleen, lung, kidney, and heart were harvested for histological investigations.

In Vivo Treatment Test

$ApoE^{-/-}$ mice on a 7-week high-fat diet were separated into three groups, each comprising 6 mice, and were subjected to treatment for 4 weeks via tail vein injections twice a week. During each injection session, the mice were anesthetized using 2% isoflurane to ensure their comfort and minimize stress. Three days after the last injection, mice were humanely euthanized using cervical dislocation while under anesthetized with 2% isoflurane (Forane) administered via inhalation, ensuring minimal distress to the animals. Nontargeted mice received Chit-IOCO-Cy5, targeted mice were given Chit-IOCO-Cy5-MTX, and the control group was administered saline. Additionally, C57BL/6 mice were given saline to serve as a baseline control. To evaluate plaque reduction and anti-inflammation, the mice's hearts and aortas were extracted. Liver, spleen, lung, and kidney were also harvested for histology studies. The aortas were divided into two parts for Western blot studies and ORO staining (Scheme S1).

Statistical Analysis of Data

Data are presented as mean standard deviation. *t* test, One-way ANOVA followed by Tukey's posthoc analysis, and Two-way ANOVA followed by Šídák multiple comparisons test were used in the analysis of significant difference. For the preparation and characterization of the nanoparticles, three individual batches were synthesized and tested individually. Subsequently, the nanoparticles were scaled up for in vitro and in vivo experiments. For the in vitro experiments, the replicate numbers reported in the figure legends represent independent cell cultures. For the in vivo experiments, the replicate numbers correspond to the number of animals included in each experimental group. More specific details are provided in figure legends. A p value of <0.05 was considered significant. Graphs were plotted using GraphPad Prism 10.

Ethical Statement of Using Human Blood

This study was conducted in full accordance with the principles outlined in the Declaration of Helsinki. Human blood used in the experiments was obtained from the Red Cross Blood Bank under human ethics approval 2021/598, which ensures that informed written consent is obtained from all donors prior to blood donation.

RESULTS

Synthesis and Characterization of the Nanocomplexes

Chit-IOCO nanocomplexes were synthesized by combining positively charged chitosan and negatively charged IO-PAA and CO-TSC in acetic acid solution. Subsequently, an EDC reaction was carried out to conjugate MTX and Cy5 dye onto Chit-IOCO. The hydrodynamic size of Chit-IOCO is approximately 180 nm, with a PDI of 0.104. Chit-IOCO displayed a positive surface zeta potential of 32.0 mV, which can be attributed to the presence of the chitosan layer (Figure 1A(iii)). Upon conjugation with Cy5 and MTX, TEM imaging revealed that the size of the Chit-IOCO-Cy5-MTX nanoparticles remained consistent at approximately 160 nm. The hydrodynamic size of the nanoparticles was similar to that of the Chit-IOCO particles, measuring around 178 nm, with a PDI of 0.118. Notably, the surface zeta potential of the Chit-IOCO-Cy5-MTX particles was reduced to 19.2 mV, which indicates the successful conjugation of Cy5 and MTX. The reduced zeta potential reflects MTX conjugation neutralizing the positive charges of chitosan. The EDS analysis of Chit-IOCO-Cy5-MTX indicates a uniform distribution of iron oxide and cerium oxide within the nanoparticles. (Figure S9). Calculation revealed that the nanoparticles were conjugated with MTX at a yield of 66.1% (eq S(1), Figure 1A(ii) and (iii)). Both Chit-IOCO and Chit-IOCO-Cy5-MTX showed exhibited good stability over a period of at least 5 days in water, saline, and saline containing 10% of serum, with no significant aggregation or degradation observed (Figure S7).

Nanocomplexes Exhibited Strong MRI Contrast Effect. Following the successful synthesis of the nanocomplexes, different iron concentrations of Chit-IOCO and Chit-IOCO-Cy5-MTX nanoparticles were prepared for use in MRI phantoms, which were subsequently scanned with a 9.4T MRI. Increasing the concentrations of iron oxide led to a reduction of T_2-weighted MR signal for both nanocomplexes. Figure 1B and Figure S1 demonstrate that Chit-IOCO-Cy5-MTX and Chit-IOCO-Cy5 exhibits more pronounced T_2 and T_2* contrast compared to Chit-IOCO, indicating that it may serve as a more sensitive T_2 contrast agent. Additionally, the graph revealed that Chit-IOCO-Cy5-MTX has higher transverse relaxivity (r_2 = 281 mM^{-1} s^{-1}, r_{2*} = 938 mM^{-1} s^{-1}) compared to Chit-IOCO (r_2 = 219 mM^{-1} s^{-1}, r_{2*} = 642 mM^{-1}

https://doi.org/10.1021/acsnanomed.5c00036
ACS Nano Med. 2026, 1, 250−267

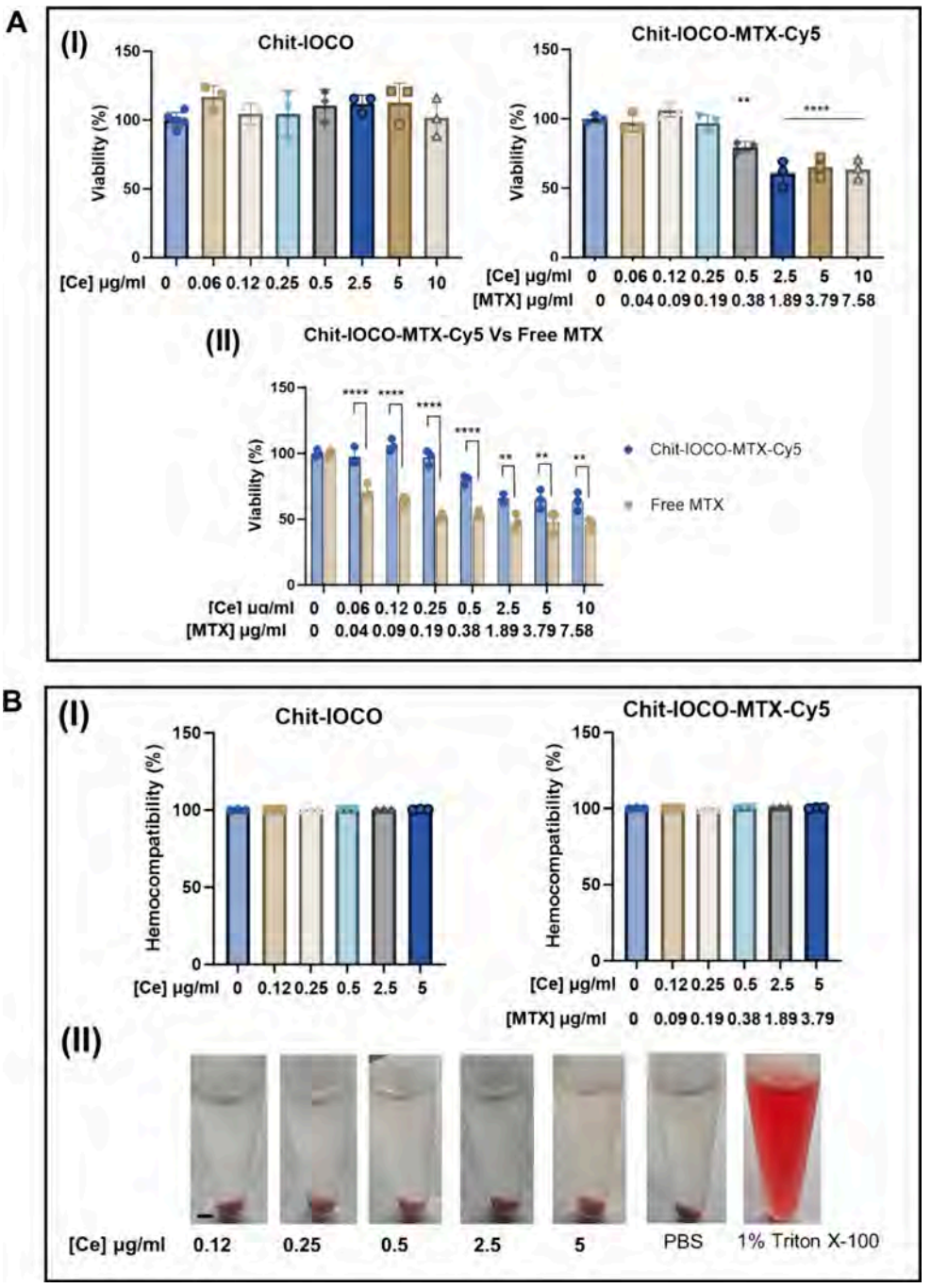

Figure 2. *In vitro* biocompatibility of nanocomplexes. (A) Viability of RAW 264.7 cells treated with nanocomplexes or free MTX at varying concentrations after 24 h incubation. (I) Viability of the RAW 264.7 cells after 24 h incubation with Chit-IOCO or Chit-IOCO-Cy5-MTX. *Compared with cell only control: $^{**}p < 0.001$, $^{****}p < 0.0001$. (II) A comparative analysis of the cellular viability between cells treated with Chit-IOCO-Cy5-MTX or treated with free MTX. *Chit-IOCO-Cy5-MTX vs free MTX: $^{**}p < 0.001$, $^{****}p < 0.0001$. (B) Hemocompatibility of Chit-IOCO and Chit-IOCO-Cy5-MTX. Human blood samples were subjected to nanocomplexes at different concentrations and incubated for a period of 4 h. A negative control was established using PBS while a positive control was established using 1% Triton-X100. After centrifugation, the plasma absorbance was measured at 545 nm. (I) The hemocompatibility of Chit-IOCO and Chit-IOCO-Cy5-MTX. (II) Images of the plasma after treated with different Chit-IOCO-Cy5-MTX. Bar = 2 mm. Statistical significance was tested by one-way ANOVA and two-way ANOVA. Mean ± S.D.*Compared with PBS control: $^{**}p < 0.01$, $^{****}p < 0.0001$, $n = 3$.

s^{-1}) hence indicating an enhanced MRI contrast ability. Furthermore, Chit-IOCO conjugated solely with Cy5 (Figure S1) also showed higher r_2 and r_2* values than Chit-IOCO (r_2 = 354.7 mM^{-1} s^{-1}, r_{2*} = 989 mM^{-1} s^{-1}). Iron oxide nanoparticles are highly effective T_2 contrast agents, inducing local magnetic field inhomogeneities that prompt dephasing of water proton spins nearby, resulting in reduced T_2 relaxation time and consequently darker images on T_2-weighted MRI scans. Conjugating methotrexate (MTX) to these nanoparticles may modify their surface characteristics and hydrodynamic dimensions, potentially influencing their relaxivity and interactions with adjacent water molecules, thereby amplifying the T_2 signal contrast.

https://doi.org/10.1021/acsnanomed.5c00036
ACS Nano Med. 2026, 1, 250−267

MTX Enhanced Cellular Uptake of Nanocomplexes. As the MRI capability of the nanocomplexes was confirmed, *in vitro* targeting ability was evaluated. RAW 264.7 cells were treated with LPS together with Chit-IOCO or Chit-IOCO-Cy5-MTX for 24 h at different cerium concentrations. RAW cells treated with Chit-IOCO-Cy5-MTX showed significantly stronger MRI T_2 effect and fluorescence signal compared to Chit-IOCO-Cy5 at a cerium concentration of 2.5 μg/mL or untreated groups (Figure 1C). The enhanced fluorescence intensity and T_2 MRI signal observed in cells treated with Chit-IOCO-Cy5-MTX indicated a greater cellular uptake facilitated by the presence of MTX.

MTX Toxicity Was Reduced When Conjugated onto Nanocomplexes. To determine the potential cytotoxic effects of the nanocomplexes on RAW264.7 macrophages, the cells were incubated with varying concentrations of the nanocomplexes or free MTX for 24 h. The viability of cells was not affected significantly by Chit-IOCO over a range of cerium concentrations from 0.06 μg/mL to 10 μg/mL. In contrast, treatment with Chit-IOCO-Cy5-MTX resulted in a reduction of cell viability to 81% at cerium concentrations of 0.5 μg/mL, with the lowest viability of 62% observed at a cerium concentration of 10 μg/mL (Figure 2A(i)). It is noteworthy that treatment of RAW cells with free MTX in the range of 0.04−0.25 ug/mL, resulted in only 50−70% of cell viability, while treatment with Chit-IOCO-Cy5-MTX at the same concentration of MTX resulted in approximately 100% cell viability. Furthermore, Chit-IOCO-Cy5-MTX exhibited approximately 20% higher cell viability than free MTX at concentrations ranging from 0.38 μg/mL to 7.58 ug/mL, indicating a significant reduction in the toxicity of free MTX following its conjugation to Chit-IOCO nanocomplexes (Figure 2A(ii) and Figure S2A). Covalent conjugation of methotrexate (MTX) to the Chit-IOCO nanoplatform substantially reduces its systemic toxicity through two main mechanisms. First, unlike free MTX—which is small in molecular weight (~454 Da) and can indiscriminately enter many cell types via reduced-folate carriers (RFC), causing off-target toxicity in liver, kidney, and gut—conjugation to a macromolecular chitosan scaffold effectively prevents recognition by RFC and restricts uptake to cells expressing folate receptor-β (FRβ) via receptor-mediated endocytosis. Second, the high molecular weight and macromolecular form of the MTX−chitosan conjugate require internalization and lysosomal processing for drug release; under physiological conditions (pH 7.4, 37 °C), free MTX release into media or circulation is negligible, minimizing extracellular toxicity and confining therapeutic activity to target cells.[39] In our system, MTX is covalently bound to chitosan via amide bonds which are highly stable, and no detectable free MTX was found in PBS supernatants, indicating a sustained intracellular release following endocytosis rather than premature extracellular release.

Overactive macrophages are major contributors to oxidative stress and inflammation, therefore reducing their number or activity can help modulate the inflammatory response. Indeed, numerous studies have shown that selectively targeting activated macrophages can be beneficial for treating inflammatory diseases.[18,19] In this context, the moderate cytotoxic effect observed at higher concentrations may contribute to therapeutic efficacy by reducing excessive macrophage-driven ROS production. On the other hand, at a lower concentration of 0.25 μg/mL, the nanoparticles significantly reduced intracellular ROS levels without inducing notable cytotoxicity. Additional cytotoxicity assays using CHO cells, a non-phagocytic epithelial-like cell line. As shown in Figure S8, treatment with 2.5 μg/mL nanoparticles did not result in significant cytotoxicity in CHO cells, supporting the selective effect of these nanoparticles on activated macrophages rather than generalized toxicity (Figure S8). This suggests a good therapeutic window, where antioxidative efficacy can be achieved while maintaining cell viability.

Conjugation of methotrexate (MTX) onto the Chit-IOCO nanoplatform endowed the nanocomplex with a folate analogue ligand function, facilitating selective binding to folate receptor-β (FRβ) expressed on activated macrophages. Consequently, FRβ-positive RAW 264.7 cells internalized MTX-modified nanoparticles more efficiently than non-MTX counterparts, which explains the significantly stronger MRI T_2 contrast and fluorescence signals observed in the Chit-IOCO-Cy5-MTX group (Figure 1C). The enhanced receptor-mediated uptake also accounts for the reduced cell viability at higher concentrations (2.5 μg mL^{-1}), as increased intracellular accumulation of cerium-oxide/iron-oxide nanoparticles together with MTX amplified suppression of pro-inflammatory cytokines but simultaneously imposed a greater cytotoxic burden. By contrast, Chit-IOCO-Cy5 exhibited only minimal cytotoxicity, consistent with its comparatively low uptake by RAW cells (Figure 2A).

To assess the suitability for clinical application, hemocompatibility of the nanocomplexes was examined (eq S(2) and S(3)). Whole blood was incubated with varying concentrations of nanocomplexes for 4 h to assess their hemocompatibility. The negative control group was treated with PBS while the positive control group was treated with 1% Triton-100X. Figure 2B and Figure S2B show no hemolysis or color changes in the whole blood treated with free MTX, Chit-IOCO, Chit-IOCO-Cy5 and Chit-IOCO-Cy5-MTX nanocomplexes, indicating that these nanocomplexes did not exhibit adverse impact on the human red blood cells.

In Vitro Anti-ROS and Anti-Inflammation Properties of Chit-IOCO and Chit-IOCO-Cy5-MTX

Cell-based anti-ROS experiments were carried out to assess the ROS scavenging activity of the nanocomplexes in RAW 264.7 cells stimulated with LPS. Macrophages were employed as the cell model in our anti-ROS efficacy experiments since they are a primary source of ROS production in various ROS and inflammatory-related disorders. LPS was utilized as a stimulant in RAW cells since it has been extensively studied and commonly used as an inducer of intracellular ROS. To investigate the scavenging of ROS, RAW cells were treated with LPS and different concentrations of either nanocomplexes or free MTX overnight.

At 0.06 μg/mL or higher concentration of cerium, Chit-IOCO-Cy5-MTX demonstrated significant ROS scavenging ability. When the cerium concentration was higher than 0.25 μg/mL, the intra cellular ROS level of macrophages was reduced to the similar level of cell-only control. At higher concentrations of Chit-IOCO-Cy5-MTX ([Ce] above 2.5 μg/mL), its potential cytotoxicity may have contributed to the lower ROS levels observed in RAW cells. Nonetheless, at cerium concentrations below 0.5 μg/mL, where little cytotoxicity was detected, Chit-IOCO-Cy5-MTX demonstrated effective anti-ROS activity. When compared to Chit-IOCO and Chit-IOCO-Cy5, these nanocomplexes were able to

https://doi.org/10.1021/acsnanomed.5c00036
ACS Nano Med. 2026, 1, 250−267

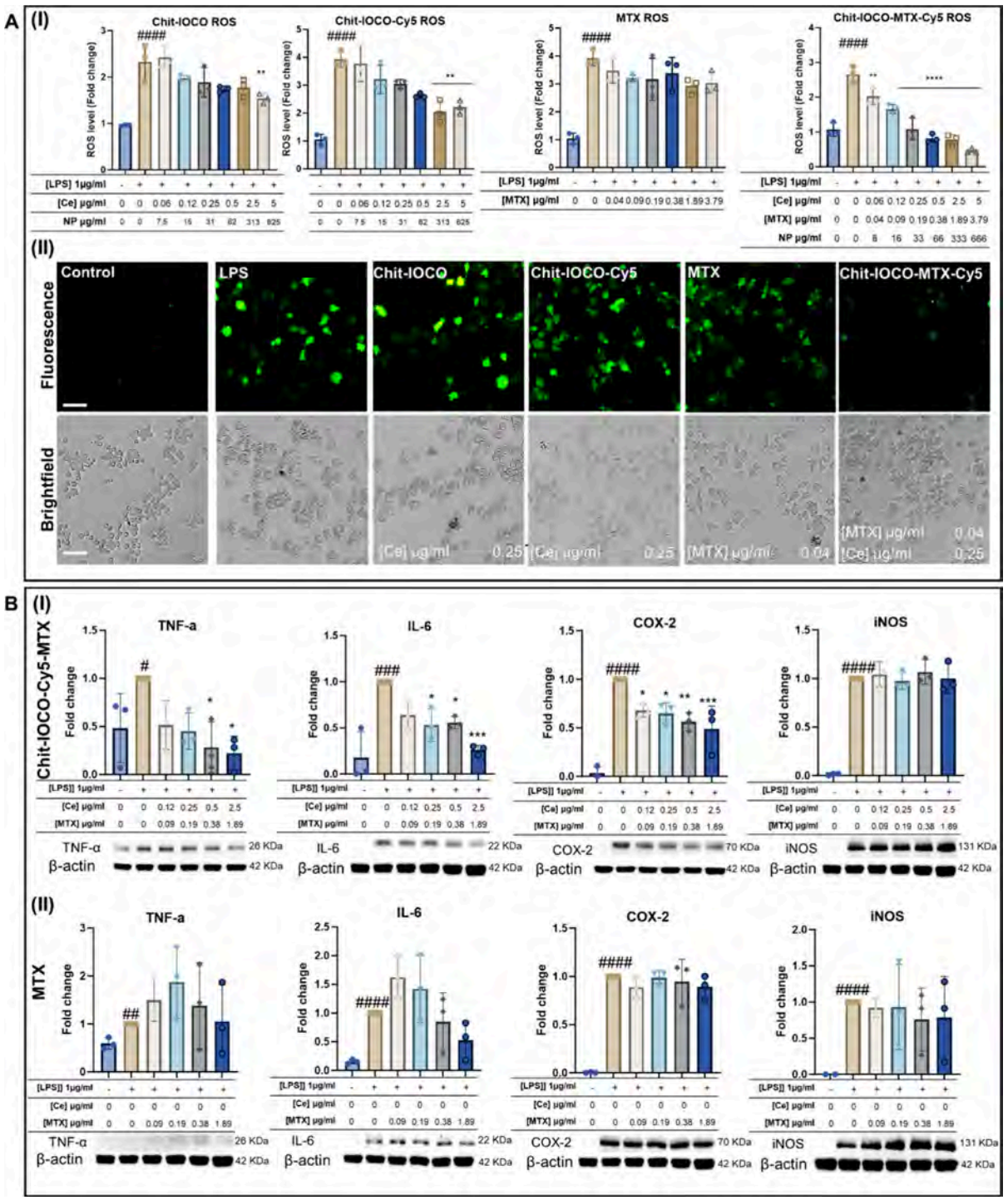

Figure 3. ROS scavenging and anti-inflammation property of nanocomplexes and free MTX in RAW 264.7 cells. (A) ROS Scavenging capacity of Chit-IOCO, Chit-IOCO-Cy5, Chit-IOCO-Cy5-MTX, and free MTX in RAW cells. (I) ROS levels in RAW cells treated with either nanocomplexes or free MTX at different concentrations. (II) Fluorescence images demonstrating ROS levels in RAW cells treated with either nanocomplexes or free MTX. Bar = 40 μm. (B) Impact of Chit-IOCO-Cy5-MTX or free MTX on the expression of inflammatory proteins in LPS-Stimulated RAW 264.7 cells. (I) Protein expression of TNF-α, IL-6, COX-2, and iNOS in RAW cells treated with Chit-IOCO-Cy5-MTX at different concentrations and LPS stimulation for 24 h. (II) Protein expression of TNF-α, IL-6, COX-2, and iNOS in RAW cells treated with free MTX at different concentrations and LPS stimulation for 24 h. Statistical significance was tested by one-way ANOVA. Mean ± S.D. *Compared with LPS control ([Ce] 0 μg/mL, [MTX] 0 μg/mL, [LPS] 1 μg/mL): *$p < 0.05$ **$p < 0.01$, ***$p < 0.001$,****$p < 0.0001$; # Compared with cell control ([Ce] 0 μg/mL, [MTX] 0 μg/mL): #$p < 0.05$ ##$p < 0.01$, ###$p < 0.001$, ####$p < 0.0001$, $n = 5-6$.

scavenge ROS at a cerium concentration higher than 0.25 μg/mL. However, their ROS scavenging efficiency was lower than Chit-IOCO-Cy5-MTX at the same cerium concentration. Besides, it is worth mentioning that free MTX did not show any ROS scavenging capability in RAW cells stimulated by LPS at all tested concentrations (Figure 3A(i)). The fluorescence microscope images (Figure 3(ii)) indicated that at the cerium concentration of 0.25 μg/mL or MTX concentrations of 0.04

https://doi.org/10.1021/acsnanomed.5c00036
ACS Nano Med. 2026, 1, 250−267

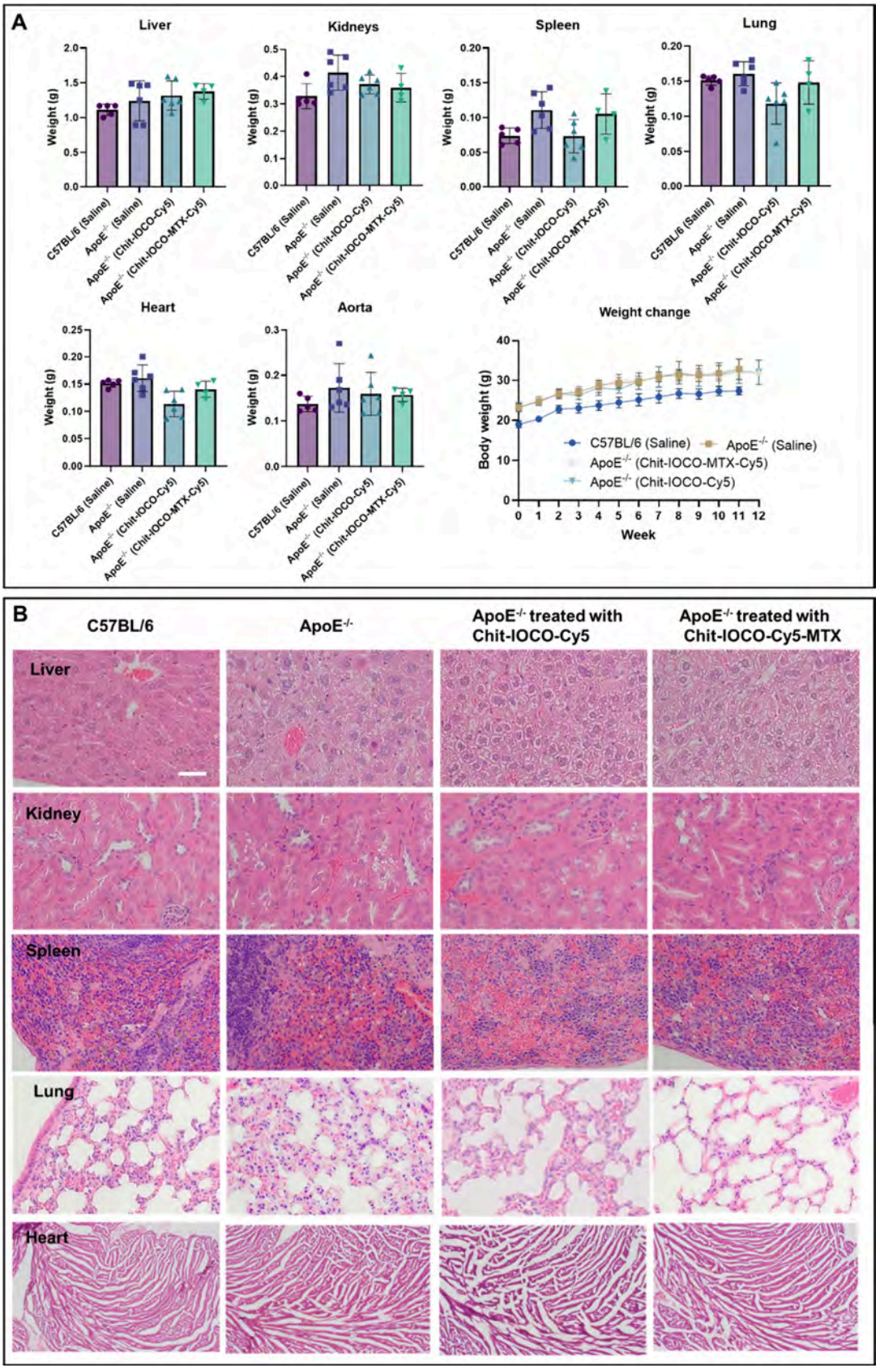

Figure 4. Effects of Chit-IOCO-Cy5 and Chit-IOCO-Cy5-MTX on weight and organs of ApoE$^{-/-}$ mice. (A) Weight of organs at end point and total body weight of ApoE$^{-/-}$ and C57BL/6 mice from Week 1 to Week 12 (n = 5−6). (B) Histological images of organs (hematoxylin and eosin (H&E) staining) 4 weeks after administration of Chit-IOCO-Cy5 or Chit-IOCO-Cy5-MTX. Bar = 20 μm.

https://doi.org/10.1021/acsnanomed.5c00036
ACS Nano Med. 2026, 1, 250−267

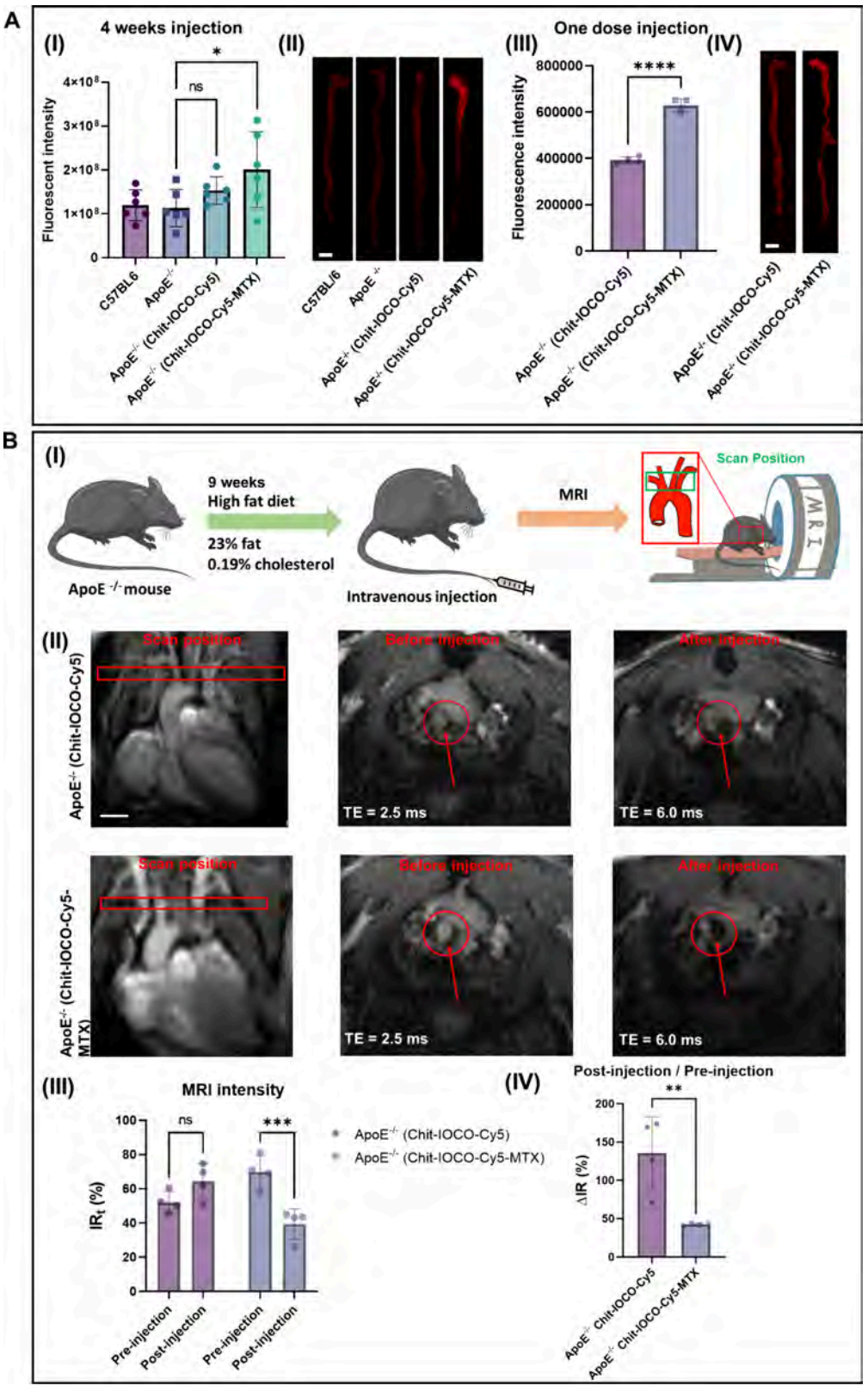

Figure 5. *In vivo* fluorescence and T_2-weighted magnetic resonance imaging (MRI) of ApoE$^{-/-}$ and C57BL/6 mice. (A) Fluorescence images of the aortas in ApoE$^{-/-}$ and C57BL/6 mice. (I) Quantification of Cy5 fluorescence intensity in aortic arches of ApoE$^{-/-}$ and C57BL/6 mice after 4-week treatment with nanocomplexes or saline (n = 6). (II) Fluorescence imaging of aortas in ApoE$^{-/-}$ and C57BL/6 mice treated with nanocomplexes or saline for 4 weeks. Bar = 2 mm. (III) Quantification of Cy5 fluorescence intensity in aortic arches of ApoE$^{-/-}$ and C57BL/6 mice after one dose treatment with nanocomplexes or saline (n = 4). (IV) Fluorescence images of aortas in ApoE$^{-/-}$ and C57BL/6 mice treated with one dose of nanocomplexes or saline. Bar = 2 mm. (B) Effects of Chit-IOCO-Cy5 and Chit-IOCO-Cy5-MTX injections on MRI T_2* image of brachiocephalic artery in ApoE$^{-/-}$ mice. (I) A scheme depicting the positioning of the aorta for MRI. (II) MRI T_2* imaging of brachiocephalic artery in ApoE$^{-/-}$ mice pre- and post-treatment with Chit-IOCO-Cy5 or Chit-IOCO-Cy5-MTX. Red cycles indicate regions of interest (ROIs),

https://doi.org/10.1021/acsnanomed.5c00036
ACS Nano Med. 2026, 1, 250−267

Figure 5. continued

and red arrows indicate the decrease in T_2* signal caused by the nanocomplexes. (III) Quantification of MRI signal intensity in the brachiocephalic artery of ApoE$^{-/-}$ mice before and after injection of Chit-IOCO-Cy5 or Chit-IOCO-Cy5-MTX. Bar = 2 mm. (IV) MRI signal intensity change ratio before and after one-day-injection of Chit-IOCO-Cy5 or Chit-IOCO-Cy5-MTX. Statistical significance was tested by one-way ANOVA and *t* test. Mean ± S.D. *p < 0.05, **p < 0.01, ***p < 0.001, ****p < 0.0001, n = 4.

μg/mL, the RAW cells treated with Chit-IOCO-Cy5-MTX had lower fluorescence intensity compared to other groups. Additionally, its fluorescence intensity considerably similar to the non-LPS treated RAW cells. Thus, these findings suggest that Chit-IOCO-Cy5-MTX has promising ROS scavenging capability.

Foam-cell formation is a hallmark of atherosclerosis, driven by excessive uptake of oxidized low-density lipoprotein (ox-LDL) by activated macrophages. To evaluate whether our nanoplatform can mitigate this process, RAW 264.7 macrophages were stimulated with LPS and subsequently exposed to ox-LDL in the presence or absence of nanoparticles. Oil Red O staining revealed a marked increase in foam-cell formation in LPS-treated cells compared with untreated controls. Notably, cotreatment with either Chit-IOCO-Cy5 or Chit-IOCO-Cy5-MTX significantly reduced the percentage of foam cells relative to LPS alone (Figure S12). Quantification was performed by determining total cell numbers using ImageJ particle counting, Oil Red O−positive cells were manually counted under microscopy. The percentage of foam cells was then calculated as the ratio of Oil Red O−positive cells to total cells. These findings demonstrate that, in addition to scavenging ROS, Chit-IOCO-Cy5 and Chit-IOCO-Cy5-MTX also inhibit macrophage transformation into foam cells, thereby targeting a critical pathogenic mechanism of atherosclerosis.

Three critical signaling pathways, namely IκB kinase (IKK) complex, c-Jun N-terminal Kinase (JNK), and p38 mitogen-activated protein kinases (p38), are integral to the synthesis of inflammatory cytokines.[40] The IKK complex related with the NF-κB pathway modulates TNF-α expression, which acts as a key mediator in both the humoral immune response and the process of apoptosis. The p38/RelA pathway, under the control of IKK complexes, is essential for the induction of IL-6.[41] Furthermore, the iNOS enzyme, known to have a significant role in the regulation of both fibrosis and sclerosis, has its expression controlled by the JNK pathway.[42] The secretion of prostaglandin E2 (PGE2) through COX-2 is guided by the p38 pathway, and the resulting PGE2 levels have a direct impact on the extent of inflammation.[43] Thus, in this study, proteins including TNF-α, iNOS, COX-2, and IL-6 were analyzed to evaluate the anti-inflammatory capabilities of the developed nanocomplexes. In order to assess the anti-inflammatory properties of Chit-IOCO-Cy5-MTX, RAW264 cells were treated with LPS (1 μg/mL) and varying concentrations of free MTX or Chit-IOCO-Cy5-MTX. Western blot technique was utilized to assess the expression levels of inflammatory proteins (TNF-α, IL-6, iNOS and COX-2). In Figure 3B(i), it can be observed that Chit-IOCO-Cy5-MTX effectively decreased the TNF-α overexpression at concentrations of MTX equal to or greater than 0.38 μg/mL. Particularly, at a concentration of 1.89 μg/mL, Chit-IOCO-Cy5-MTX resulted in a significant decrease of TNF-α secretion to a level comparable to that observed in the cell control group. Additionally, Chit-IOCO-Cy5-MTX demonstrated a decrease in the expression of IL-6 at a concentration of 0.19 μg/mL of MTX, and when the MTX concentration reached 1.89 μg/mL, it showed similar levels of IL-6 in the cell control group. Furthermore, Chit-IOCO-Cy5-MTX displayed a significant decrease in COX-2 expression at MTX concentrations of 0.09 μg/mL and above. At the concentration of 1.89 μg/mL, Chit-IOCO-Cy5-MTX suppressed COX-2 secretion by approximately 50% compared to LPS-stimulated groups. Notably, Chit-IOCO-Cy5-MTX did not exhibit any inhibitory effects on iNOS production. Interestingly, as illustrated in Figure 3B(ii), the administration of free MTX did not lead to any statistically significant inhibition of the production of these four types of proteins.

Biocompatibility of Chit-IOCO-Cy5-MTX and Chit-IOCO-Cy5 in a Mouse Model

Our study employed ApoE$^{-/-}$ mice fed with a high-fat diet, which is a commonly used model for atherosclerosis and closely resembles the human pathology.[44] C57BL/6 mice were included as a control group. The ApoE$^{-/-}$ mice were fed with a high-fat diet for a total of 11 weeks and were intravenously injected with Chit-IOCO-Cy5 or Chit-IOCO-Cy5-MTX twice a week for 4 weeks after 7 weeks of high-fat diet treatment. As a negative control group, C57BL/6 mice were fed a normal diet and injected with saline intravenously twice a week for 4 weeks starting from week 7. The weight of the mice was regularly monitored prior to injections. ApoE$^{-/-}$ mice fed with a high-fat diet showed faster weight gain compared to C57BL/6 mice. However, there was no significant difference observed in weight changes among the ApoE$^{-/-}$ groups from week 1 to week 11 (Figure 4A). At the end of week 11, the major organs including liver, spleen, kidney, heart, and lung were collected and weighed. Treatment with Chit-IOCO-Cy5-MTX did not result in a significant difference in the weight of all organs compared to C57BL/6 mice and nontreated ApoE$^{-/-}$ mice. However, ApoE$^{-/-}$ mice treated with Chit-IOCO-Cy5 showed a slight decrease in the weight of the lung and heart (Figure 4A). In addition, ex vivo biodistribution was investigated by fluorescence imaging of major organs at 48 h postinjection. As shown in Figure S11, Chit-IOCO-Cy5-MTX nanoparticles predominantly accumulated in the liver and kidneys, consistent with the well-recognized clearance routes of nanoparticle systems. (Figure S11)

Thin sections of organs were taken and stained with H&E for microscopic examination. The images (Figure 4B) revealed no significant differences or lesions between the organs of nontreated ApoE$^{-/-}$ mice and those treated with the nanocomplexes. However, the high-fat diet treatment resulted in fatty livers in ApoE$^{-/-}$ mice. In summary, Chit-IOCO-Cy5-MTX did not have a significant effect on the weight of ApoE$^{-/-}$ mice or their organs.

Chit-IOCO-Cy5-MTX Improved Targeting and Enhanced MRI Contrast in Atherosclerosis Mouse Model

In this experiment, we evaluated the targeting efficacy and MRI contrast capabilities of chitosan nanocomplexes, following both long-term and single-dose intravenous administration (Figure 5B(i)). For long-term injection, The ApoE$^{-/-}$ mice were subjected to a 7-week high-fat diet and subsequently

https://doi.org/10.1021/acsnanomed.5c00036
ACS Nano Med. 2026, 1, 250−267

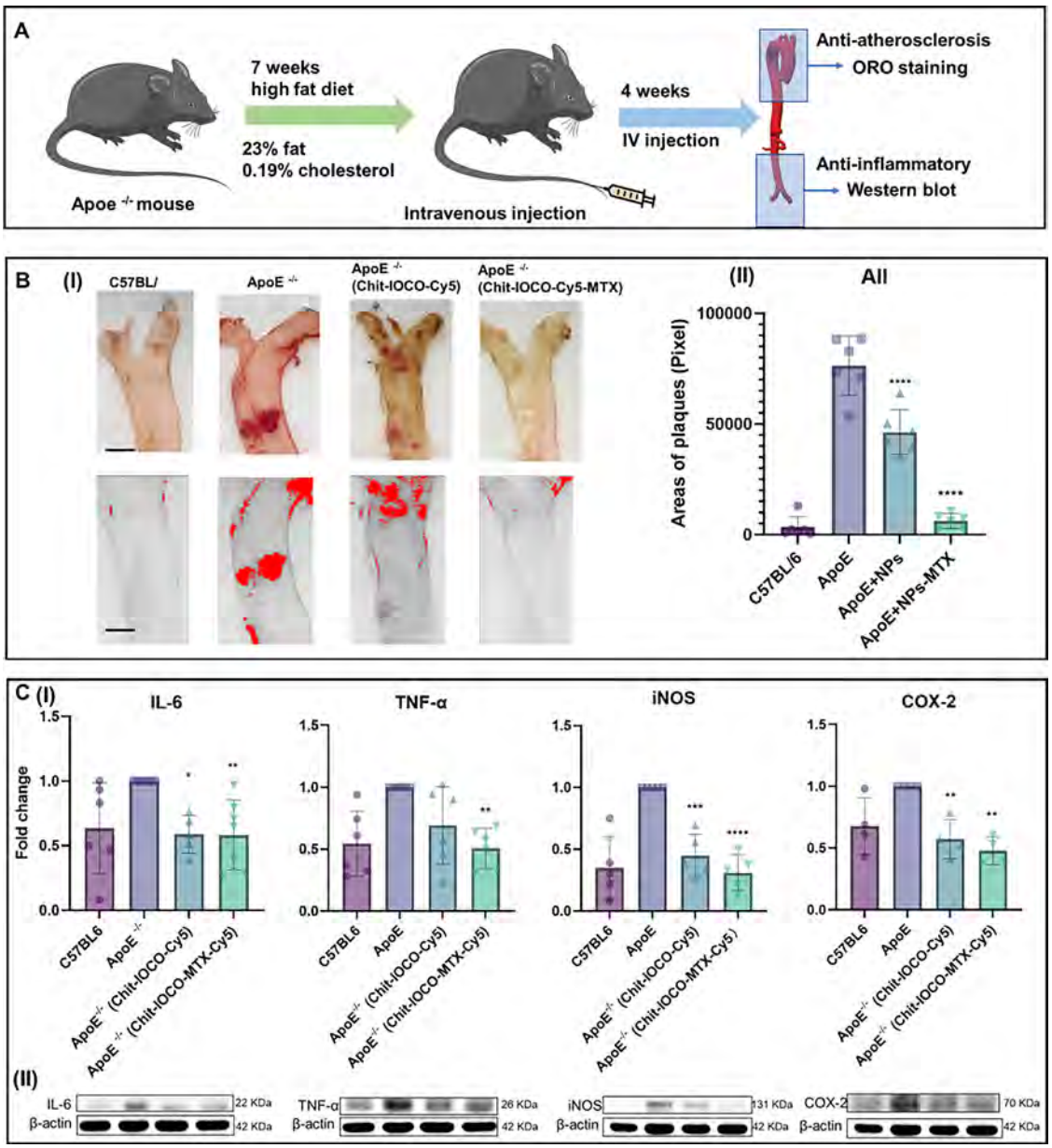

Figure 6. ApoE$^{-/-}$ mice treatment with Chit-IOCO-Cy5 and Chit-IOCO-Cy5-MTX. (A) A scheme depicting the positioning of the aorta for ORO staining and Western blot analysis. (B) ORO staining of aortic arches. (I) The ORO staining images of the aortic arches (upper panel) and the region of interest (ROI) (red) of the atherosclerotic plaques (lower panel) in ApoE$^{-/-}$ mice that were administered Chit-IOCO-Cy5, Chit-IOCO-Cy5-MTX, or saline for 4 weeks were analyzed. As a negative control, C57BL/6 mice were injected with saline for the same duration. Bar = 1 mm. (II) Quantification of the atherosclerotic plaque area for the aortic arch. (C) Chit-IOCO-Cy5 and Chit-IOCO-Cy5-MTX decreasing the overexpression of inflammatory proteins in the lower abdominal aortas of ApoE$^{-/-}$ mice. (I) IL-6, TNF-α, iNOS, and COX-2 protein levels normalized to β-actin. (II) Images representing Western blot for IL-6, TNF-α, iNOS, and COX-2 and β-actin. Statistical significance was tested by one-way ANOVA followed by Tukey's posthoc analysis. Mean ± S.D. *$p < 0.05$, **$p < 0.01$, ***$p < 0.001$, ****$p < 0.0001$, $n = 4–6$, compared to nontreated ApoE$^{-/-}$ mice.

administered intravenous injections of saline (positive control), Chit-IOCO-Cy5 or Chit-IOCO-Cy5-MTX twice per week for 4 weeks together with high-fat diet treatment. A negative control group of C57BL/6 mice, fed a normal diet, received intravenous injections of saline twice per week for 4 weeks starting from the seventh week of high-fat diet. At week 11, the mice were euthanized, and their aortas were collected and subjected to ex vivo processing. Before the administration of the nanocomplexes, initial MRI scans were conducted to establish a baseline. Subsequent MRI scans were performed 1 day following the injection. After imaging, the mice were euthanized, and their aortas were collected and subjected to ex vivo processing. Figure 5A(i, ii) displays a noteworthy increase in the fluorescence signal in the aortic arches of ApoE$^{-/-}$ mice treated with Chit-IOCO-Cy5-MTX in comparison to the untreated ApoE$^{-/-}$ group. In contrast, no significant difference was observed between the untreated ApoE$^{-/-}$ group and the group treated with Chit-IOCO-Cy5.

To evaluate the targeting ability of Chit-IOCO-Cy5-MTX after a single-dose intravenous administration, ApoE$^{-/-}$ mice were fed a high-fat diet for 9 weeks and given a single injection of either Chit-IOCO-Cy5 or Chit-IOCO-Cy5-MTX. After 24

https://doi.org/10.1021/acsnanomed.5c00036
ACS Nano Med. 2026, 1, 250−267

h, the mice were sacrificed, and their aortas were harvested and subjected to ex vivo fluorescence scanning. Prior to performing MRI, the optimal imaging window was systematically evaluated using in vivo fluorescence imaging (IVIS) at different time intervals (1 h, 1 day, 2 days, and 3 days postinjection). As shown in Figure S10, fluorescence signal intensity within the atherosclerotic lesions reached its maximum at 24 h post-injection. Accordingly, this time point was selected for subsequent MRI experiments.

Results indicated that mice treated with Chit-IOCO-Cy5-MTX exhibited a higher fluorescence intensity in their aortic arches compared to those treated with Chit-IOCO-Cy5. These findings suggest that Chit-IOCO-Cy5-MTX exhibits superior targeting ability compared to Chit-IOCO-Cy5, presumably due to the presence of MTX which targets the folic acid receptor on the atherosclerosis.

In addition to fluorescence imaging, the MRI intensity of the brachiocephalic artery of ApoE$^{-/-}$ mice was examined by acquiring MRI (PD/T2*) intensity ratio (IR_t) before and after administration of the nanocomplexes (eqs S(4) and S(5)). The short TE (2 ms) produced proton density (PD)-weighted images, whereas the long TE (6 ms) produced T2*-weighted images. A significant difference in ΔIR (Figure 5B(ii) and (iii)) was observed between pre- and 1-day postinjection of Chit-IOCO-Cy5-MTX, whereas ApoE$^{-/-}$ mice treated with Chit-IOCO-Cy5 did not show any significant signal change. The lower ΔIR ratio showed an enhanced darkening MRI signal within ROI, indicating a preferential accumulation of Chit-IOCO-Cy5-MTX in the brachiocephalic artery of ApoE$^{-/-}$ mice compared to Chit-IOCO-Cy5 (Figure 5B(iii)). Additionally, Figure 5B(ii) demonstrates a decrease in T_2*-weighted signal in atherosclerotic plaques in the brachiocephalic artery, suggesting that Chit-IOCO-Cy5-MTX could be a useful MRI contrast agent for detecting atherosclerotic plaques.

Reduction of Plaque Area and Inflammatory Protein Expression by Chit-IOCO-Cy5-MTX in Atherosclerosis Mouse Model

Upon confirmation of the accumulation of Chit-IOCO-Cy5-MTX in plaques, the effect of these nanocomplexes on the progression of plaque in ApoE$^{-/-}$ mice was evaluated. Four groups (6 mice per group) were used in the experiment, including ApoE$^{-/-}$ mice treated with saline (positive control), C57BL/6 mice treated with saline (negative control), and ApoE$^{-/-}$ mice treated with Chit-IOCO-Cy5, and Chit-IOCO-Cy5-MTX. All the mice were kept on a high-fat diet throughout the study, and the plaque area was determined by staining with ORO. Representative images and ROIs of stained aortas from the four groups are shown in Figure 6B(i) and Figures S3, S4, and S6, and the plaque area in the aortic arch was quantified in Figure 6B(ii) and Figures S3 and S4. The results revealed a significant reduction in plaque area in both nanocomplex groups when compared to the saline group, with Chit-IOCO-Cy5-MTX displaying a greater reduction than Chit-IOCO-Cy5. Furthermore, Chit-IOCO-Cy5-MTX-treated ApoE$^{-/-}$ mice exhibited almost no plaque at the aorta root, thoracal aorta and abdominal aorta.

Western blot results depicted in Figure 6C show that both Chit-IOCO-Cy5 and Chit-IOCO-Cy5-MTX reduce the overexpression of IL-6, iNOS, and COX-2 ([MTX], 1 mg/kg). However, Chit-IOCO-Cy5-MTX exhibited a more substantial reduction of these proteins. Moreover, Chit-IOCO-Cy5-MTX decreased the protein expression of TNF-α, while this effect was not observed with Chit-IOCO-Cy5. The change in serum malondialdehyde level (Figure S5), a biomarker of lipid peroxidation and oxidative stress,[45] was not observed in our mice model, indicating that nanoparticle treatment did not affect oxidized cholesterol level.

DISCUSSION

In this investigation, we utilized the electrostatic self-assembly technique to fabricate nanocomplexes comprising positively charged chitosan, and negatively charged ceria, and iron oxide. Chitosan, an amino polysaccharide derived from the deacetylation of chitin under alkaline conditions, has found extensive applications in diverse fields including drug delivery and cell culture.[46] Here, chitosan was utilized as a carrier to encapsulate both nanoceria and iron oxide nanoparticles, resulting in Chit-IOCO with a size of around 160 nm that are appropriate for biological applications. Labeling Chit-IOCO with MTX enhanced its accumulation in macrophages in vitro and in the atherosclerotic aortas in vivo as demonstrated by fluorescence imaging and MRI.

Reproducibility and Scalability of the Synthesis of the Nanoparticles

The synthesis of the Chit-IOCO-Cy5-MTX nanocomplexes exhibited excellent reproducibility. Across multiple batches, the nanoparticles showed consistent physicochemical characteristics, including uniform size distribution (with diameter variations within ±5 nm) and stable zeta potentials (variation < ±3 mV), indicating good batch-to-batch reproducibility. These results demonstrate the robustness of our electrostatic self-assembly method.

Regarding scalability, we note that the synthesis was performed in small-volume, multibatch formats, rather than by simply doubling or multiplying the reagent quantities in a single reaction vessel. This approach was adopted to maintain uniform mixing and precise control over reaction kinetics, which can be difficult to replicate in larger-scale single-pot reactions. While this method is suitable for generating the quantities needed for in vivo animal studies, we recognize that transitioning to large-scale production for clinical translation may require further process optimization, such as controlled mixing systems or microfluidic synthesis to maintain particle uniformity and consistency.

Conjugation of MTX to Chit-IOCO-Cy5 Resulted in Enhanced Reduction of ROS and Inflammatory Protein Expression

Conjugation of MTX to the nanocomplexes resulted in an enhancement of their anti-inflammation and anti-ROS properties, probably due to the enhanced cell uptake of MTX-conjugated Chit-IOCO thanks to the presence of MTX.

MTX functions dually as a folate receptor-targeting ligand and anti-inflammatory agent, exploiting the overexpression of FR-β on activated macrophages in atherosclerotic plaques. This is based on two well-supported properties. First, MTX selectively binds to folate receptors (FR), particularly FR-β, which are highly overexpressed on activated macrophages—a key cellular player in the progression of atherosclerosis. Studies have confirmed that FR-β is upregulated at inflammatory sites, including atherosclerotic lesions, similar to its role in rheumatoid arthritis and other chronic inflammatory conditions. This enables MTX to facilitate receptor-mediated endocytosis, enhancing site-specific nanoparticle uptake.[47,48]

https://doi.org/10.1021/acsnanomed.5c00036
ACS Nano Med. 2026, 1, 250−267

Second, MTX has demonstrated anti-inflammatory efficacy by suppressing pro-inflammatory cytokines (e.g., IL-6, TNF-α) and macrophage activation, both of which are central to plaque destabilization and progression.[49] Although free MTX shows limited efficacy in cardiovascular trials such as CIRT, this is likely due to systemic under-targeting, which we address through nanoparticle-mediated delivery.[50] Hence, the conjugation of MTX provides a "two-in-one" mechanism to improve lesion-specific accumulation and therapeutic impact, optimizing both precision and efficacy in atherosclerosis management.

As discussed earlier, the effectiveness of cerium oxide in reducing ROS levels is largely dependent on the surface valence of the nanoparticles. Cerium oxide can exist in two oxidation states, Ce^{3+} and Ce^{4+}, and the relative proportion of surface Ce^{3+} has a significant impact on its anti-ROS effect.[12,51] Our previous study[14] demonstrated that the ROS level in cells treated with Chit-IOCO at 10 μg/mL of cerium was comparable to control cells. Interestingly, our previous studies in oncology employing Chit-IOCO-Cy5-MTX revealed a dual behavior of cerium oxide nanoparticles depending on the cellular context.[52] In tumor cells, which intrinsically maintain high ROS levels, Chit-IOCO-Cy5-MTX treatment further increased intracellular ROS, thereby promoting apoptosis and suppressing tumor growth. In contrast, in endothelial cells, Chit-IOCO-Cy5-MTX reduced ROS level. In this atherosclerosis study, we further demonstrated that in activated macrophages, Chit-IOCO-Cy5-MTX nanoparticles reduced ROS levels and downregulated inflammatory cytokine release. These represent fundamentally distinct therapeutic logics—ROS upregulation for cancer therapy versus ROS downregulation for atherosclerosis—which highlight the versatility of CeO_2-based platforms across different disease settings. Endothelial dysfunction is a critical contributor to atherogenesis. These finding further supports the vascular-protective potential of Chit-IOCO-Cy5-MTX.[52] The dual regulatory behavior of CeO_2 in modulating reactive oxygen species can be explained by its reversible Ce^{3+}/Ce^{4+} redox cycling and pH-dependent enzyme-mimetic activities. The coexistence of Ce^{3+} and Ce^{4+} on the nanoparticle surface allows CeO_2 to function as both a superoxide dismutase (SOD)- and catalase (CAT)-mimetic nanozyme, continuously converting between oxidation states to maintain redox balance. Under near-neutral physiological conditions, such as in activated macrophages or endothelial cells, both SOD- and CAT-like reactions proceed efficiently, converting superoxide radicals to hydrogen peroxide and subsequently to water and oxygen, thereby restoring redox homeostasis and suppressing NF-κB/MAPK-driven inflammation. In contrast, in the acidic and ROS-rich tumor microenvironment, the CAT-like activity of CeO_2 is significantly reduced while the SOD-like reaction dominates, resulting in the accumulation of hydrogen peroxide and amplified oxidative stress that exceeds the apoptotic threshold. Thus, CeO_2 acts as a redox-adaptive nanozyme, functioning as an antioxidant in inflammatory macrophages and endothelial cells, but as a pro-oxidant in tumor cells, consistent with our previous oncology findings and the current atherosclerosis study.[12,53] Moreover, we found that the surface modification of Chit-IOCO with MTX and Cy5 resulted in the development of Chit-IOCO-Cy5-MTX with significantly enhanced anti-ROS ability (100% scavenging), even at a lower concentration of cerium (0.5 μg/mL). Notably, MTX alone did not show any anti-ROS effect at the concentrations tested in our study (up to 3.79 μg/mL).

In this study, it was observed that free MTX did not significantly reduced TNF-α, IL-6, COX-2 and iNOS expression at concentrations up to 1.89 μg/mL. In literature, however, anti-inflammation capability of MTX was reported but at much higher concentrations than those in our study. For example, Park et al. demonstrated the potential of MTX as an anti-inflammatory agent[54] by reducing TNF-α expression in IFN-γ or LPS-induced RAW 264.7 macrophages at concentrations of 454 μg/mL.

Regarding Chit-IOCO, in our previous studies,[15] Chit-IOCO only exhibited a 20% reduction in TNF-α expression (1 μg/mL of cerium) and COX-2 expression (10 μg/mL of cerium). Here, Chit-IOCO-Cy5-MTX conjugates demonstrated more than 90% reduction in TNF-α expression when cerium concentration reached 0.5 μg/mL and a 40% reduction in COX-2 expression at a cerium concentration of 0.12 μg/mL. This indicates that Chit-IOCO-Cy5-MTX was able to effectively reduce the overexpression of TNF-α and COX-2 at lower concentrations, indicating improved performance. Furthermore, the conjugation of MTX to Chit-IOCO-Cy5 not only improved the reduction of TNF-α and COX-2 expression at lower concentrations, but also enhanced the inhibition of IL-6 expression. Specifically, Chit-IOCO-Cy5-MTX was found to inhibit IL-6 expression by 40% at a cerium concentration of 0.25 μg/mL and by 80% at a cerium concentration of 2.5 μg/mL while free MTX (this study) and Chit-IOCO (our previous study)[15] did not show significant reduction of IL-6 expression.

Interestingly, the conjugation of methotrexate (MTX) to chitosan-based Chit-IOCO-Cy5 has been shown to effectively reduce the drug's toxicity. It is probably because MTX was no longer present as a small molecule drug but as a large MTX-chitosan construct, which changes its pharmacokinetics.

Chit-IOCO-Cy5-MTX Exhibited Stronger *In Vitro* Anti-Inflammation Effect than Other Reported Cerium Oxide Nanoparticles

Cerium oxide nanoparticles have been reported to exhibit anti-inflammatory properties by other studies. For example, Ban et at.[55] found that nanoceria ([Ce] - 500 μg/mL) reduced TNF-α and iNOS by 50% in LPS activated RAW 264.7 cells. Similarly, Selvaraj et al.[56] reported that at 7 μg/mL of cerium, cerium oxide nanoparticles significantly attenuated the expression of pro-inflammatory proteins including iNOS, IL-6, COX-2 and TNF-α by approximately 20%, 30%, 20%, and 30%, respectively, in LPS-stimulated RAW264.7 cells. It is noteworthy that the anti-inflammatory effects of the nanocomplexes demonstrated in our study are better than cerium oxide nanoparticles reported in previous studies. In our study, we evaluated the anti-inflammatory potential of Chit-IOCO-Cy5-MTX in LPS-stimulated RAW264.7 macrophages. At a concentration of 2.5 μg/mL of cerium, Chit-IOCO-Cy5-MTX was found to have a stronger anti-inflammatory effect than previous studies, as it notably down-regulated TNF-α by 90%, IL-6 by 80% and COX-2 by 50% protein expression. However, the nanocomplexes did not exhibit any inhibitory effect on iNOS expression at 2.5 μg/mL of cerium. Overall, these findings suggest the potential of Chit-IOCO-Cy5-MTX as a powerful candidate for reducing inflammation cytokines' overexpression.

https://doi.org/10.1021/acsnanomed.5c00036
ACS Nano Med. 2026, 1, 250−267

Significant Reduction of Plaque Area and Inflammatory Protein Expression Achieved by Chit-IOCO-Cy5-MTX in *In Vivo* Atherosclerosis Model

In this section, we aim to compare the effectiveness of our Chit-IOCO-Cy5-MTX nanoparticles with previously reported nanoparticles for the treatment of atherosclerosis. It is important to note that our study investigated the combination of cerium oxide nanoparticles (CeO_2) and methotrexate (MTX) for atherosclerosis treatment, which, to the best of our knowledge, is a novel approach not previously reported in the literature. This unique combination sets our research apart from prior studies. Subsequently, we investigated the therapeutic and diagnostic effects of Chit-IOCO-Cy5-MTX in an *in vivo* atherosclerosis model. To assess the effectiveness of these nanocomplexes, we evaluated plaque area in the aorta root, which is a common site for atherosclerotic plaque deposition.[57] Additionally, we also analyzed the expression of inflammatory proteins in the lower abdominal region[58] of the mice aorta. Our findings demonstrated that Chit-IOCO-Cy5-MTX administration significantly reduced the overexpression of IL-6, iNOS, and COX-2 after a four-week treatment regimen ([MTX], 1 mg/kg; [Ce], 1.3 mg/kg; [Fe], 1.2 mg/kg), suggesting its potential as a therapeutic and diagnostic agent for atherosclerosis. Furthermore, the treated mice showed almost no plaque formation in the aorta root, indicating the efficacy of Chit-IOCO-Cy5-MTX in preventing atherosclerosis progression.

Methotrexate (MTX) is uniquely suited for dual-function use in our nanocomplex: as both a targeting ligand and an anti-inflammatory agent. This is based on two well-supported properties. First, MTX selectively binds to folate receptors (FR), particularly FR-β, which are highly overexpressed on activated macrophages—a key cellular player in the progression of atherosclerosis. Studies have confirmed that FR-β is upregulated at inflammatory sites, including atherosclerotic lesions, similar to its role in rheumatoid arthritis and other chronic inflammatory conditions (Low et al., 2020). This enables MTX to facilitate receptor-mediated endocytosis, enhancing site-specific nanoparticle uptake. Second, MTX has demonstrated anti-inflammatory efficacy by suppressing pro-inflammatory cytokines (e.g., IL-6, TNF-α) and macrophage activation, both of which are central to plaque destabilization and progression (Cutolo et al., 2021). Although free MTX shows limited efficacy in cardiovascular trials such as CIRT, this is likely due to systemic under-targeting, which we address through nanoparticle-mediated delivery. Hence, the conjugation of MTX provides a "two-in-one" mechanism to improve lesion-specific accumulation and therapeutic impact, optimizing both precision and efficacy in atherosclerosis management. Previous studies have demonstrated that free MTX (1 mg/kg) did not result in a statistically significant difference in plaque coverage when compared to the saline group, while their MTX-loaded nanoparticles showed only half plaque coverage compared to positive control groups.[59] Similarly, Frabcesco et al.[60] using higher concentrations of MTX (2.5 mg/kg) reported that the mice treated with MTX-liposomes (LIP) nanoparticles had around 50% reduction of aortic sinus plaque compared to the control mice. In addition, they observed a decrease in the levels of IL-6 and TNF-α in the serum samples of mice treated with MTX-LIP. Compared with these MTX-LIP, our nanocomplexes have shown outstanding results, reducing more than 95% of plaque at the concentration of MTX as low as 1 mg/kg. These findings suggest that our nanocomplexes exhibit greater therapeutic potential of atherosclerosis compared to other MTX related nanoparticles, even at significantly lower MTX concentrations.

In addition to the use of MTX-loaded nanoparticles for atherosclerosis treatment, cerium oxide nanoparticles have also been studied in the ApoE$^{-/-}$ mice model. Wang et al.[16] reported a more than 90% reduction in aortic plaque when mice were treated with 150 mg/kg of their cerium-loaded nanoparticles for 8 weeks. Similarly, Wen et al.[61] found that after a four-week treatment of their molecularly imprinted ceria nanocomposites at a cerium concentration of approximately 7 mg/kg, the plaque area had more than 50% of reduction than the control mice. Compared with these ceria-loaded nanoparticles, our nanocomplexes reduced more than 95% of plaque at the concentration of cerium at only 1.3 mg/kg. This significant reduction in atherosclerosis plaque indicating the exceptional therapeutic potential of our nanocomplexes on atherosclerosis when compared to cerium-loaded nanoparticles in previous studies.

Unlike earlier studies that focused primarily on ROS regulation or plaque area,[17] our in vivo analysis provided direct evidence that the nanoplatform mitigated inflammatory cytokine expression within plaques, confirming anti-inflammatory activity at the lesion site. In our earlier works,[10,13,14] we explored various theranostic platforms combining ceria and iron oxide. However, these nanosystems have not yet been applied to atherosclerosis. The present study is the first to investigate a theranostic platform integrating iron oxide and cerium oxide for the treatment of atherosclerosis. Despite the promising therapeutic outcomes of Chit-IOCO-Cy5-MTX, several limitations should be acknowledged. First, long-term biodistribution, accumulation, and potential toxicity require further longitudinal studies to establish safety. Second, although conjugation of methotrexate (MTX) increased anti-inflammatory effects, its broader impact on normal immune cells remains to be clarified. Third, the current work is limited to ApoE$^{-}/^{-}$ murine models; validation in additional preclinical models and direct comparison with existing therapeutics are necessary to strengthen translational relevance. Future studies could further enhance the translational impact of this theranostic nanoplatform. One promising avenue is its integration with real-time biosensing technologies, enabling continuous monitoring of inflammatory biomarkers relevant to atherosclerosis.[62] Another direction is the use of microfluidic-assisted synthesis, which offers precise and scalable control over nanoparticle formulation, thereby improving reproducibility and clinical potential.[63] Finally, comparative analyses with other drug delivery nanosystems, including polymeric, lipid-based, or biomimetic carriers, will help clarify the relative advantages of ceria-based nanoplatforms and guide rational optimization for vascular disease therapy.[64] Additionally, future studies can incorporate histological and immunohistochemical staining including hematoxylin and eosin (H&E), CD68, MMP-9, and α-SMA staining, to further characterize lesion morphology, immune cell infiltration, and extracellular matrix remodelling. These efforts will enable a more complete understanding of the therapeutic impact of Chit-IOCO-Cy5-MTX nanoparticles on atherosclerosis and provide stronger mechanistic evidence.

In summary, our study introduces a Chit-IOCO-Cy5-MTX nanocomplexes, not only in comparison to MTX-loaded nanoparticles but also in comparison to cerium-loaded

https://doi.org/10.1021/acsnanomed.5c00036
ACS Nano Med. 2026, 1, 250−267

nanoparticles, further highlighting the potential of our innovative approach as a therapeutic agent for atherosclerosis.

Potential of Chit-IOCO-Cy5-MTX as Outstanding Iron-Based MRI Contrast Agent for Atherosclerosis Diagnosis

In addition to its therapeutic potential, the Chit-IOCO-Cy5-MTX nanocomplex was designed for dual-functionality as a diagnostic agent for atherosclerosis. To enable noninvasive imaging, ultrasmall superparamagnetic iron oxide nanoparticles (USPIONs) were employed as contrast agents for magnetic resonance imaging (MRI). In recent years, USPIONs have shown significant potential for diagnosing various diseases, including inflammatory conditions[65] and cancer.[66] In comparison to commonly used gadolinium-based MRI contrast agents, USPIONs have reduced toxicity and longer circulation times, making them a safer option for patients.[67] Furthermore, USPIONs exhibit superior MRI contrast efficiency when compared to the commercial iron-based MRI contrast agent Feridex I.V., making them a more attractive alternative for diagnostic imaging purposes.[68,69]

In this study, we determined the transverse relaxivity (r_2) of Chit-IOCO-Cy5-MTX at 9.4T, which showed the MRI T_2 contrast ability of the MRI agent. Our findings indicated that the transverse relaxivity of these nanocomplexes (281 $mM^{-1}s^{-1}$) was stronger compared to those of clinical iron oxide contrast agents, such as FeREX (r_2 = 284 at 9.4 T, r_2 = 160 at 3 T), Feridex (r_2 = 307 at 9.4 T, r_2 = 93 at 3 T), and Resovist (r_2 = 143 at 3 T), as reported in previous studies.[70]

In addition to its favorable transverse relaxivity, Chit-IOCO-Cy5-MTX was found to exhibit strong MRI T_2* contrast ability, enabling the detection of the nanoparticle delivery to the atherosclerotic plaque in $ApoE^{-/-}$ mice. Notably, MRI signal in the brachiocephalic atherosclerotic plaque was observed after a single dose injection at 1.2 mg Fe/kg, indicating the potential for effective monitoring of the nanoparticle's delivery to the targeted site. The MRI results obtained in this study indicate that Chit-IOCO-Cy5-MTX has strong potential as an effective MRI contrast agent for the detection of atherosclerosis.

In addition to validating the efficacy of our Chit-IOCO-Cy5-MTX system, it is worth noting that the material formulation itself may provide opportunities for further optimization. Previous studies have demonstrated that mixed oxides can outperform their single-component counterparts. For instance, $MnFe_2O_4$–Fe_3O_4 core–shell nanoparticles exhibit markedly higher T_2 relaxivity than either component alone, while Mn-doped CeO_2 enhances oxygen vacancy formation and strengthens ROS regulation relative to pure CeO_2. These findings highlight that the ratio and type of oxides incorporated can substantially alter both imaging and therapeutic performance. Although a systematic screening of alternative combinations such as MnO/FeO or CeO_2/CoO was beyond the scope of the present work, our results underscore the potential of the current platform and highlight future opportunities to explore how varying oxide compositions and modular designs may further optimize the balance between anti-inflammatory efficacy and imaging sensitivity in the treatment of atherosclerosis.

LIMITATIONS AND TRANSLATIONAL OUTLOOK

This study provides evidence that the cerium oxide/iron oxide-based theranostic nanocomplex (Chit-IOCO-Cy5-MTX) can effectively modulate oxidative stress and inflammation in a murine model of atherosclerosis. However, several limitations should be acknowledged. First, the systemic biosafety, long-term biodistribution, and clearance of the material have not yet been comprehensively assessed. Although no apparent toxicity was observed in major organs at the tested dose, future work should include GLP-compliant toxicology, immunogenicity, and pharmacokinetic studies to confirm the translational safety of the formulation. Second, the present study did not include direct head-to-head comparisons with clinically used anti-atherosclerotic drugs such as statins or colchicine. Such comparative studies would help to benchmark the therapeutic efficacy and dosing advantage of the nanocomplex against current pharmacological standards. Moreover, the current work represents a murine proof-of-concept model, which does not yet meet the requirements for clinical translation. Large-animal studies with human-like hemodynamics and vascular physiology will be essential to validate efficacy, biosafety, and MRI-guided imaging performance under clinically relevant conditions. Finally, scalable manufacturing and batch-to-batch reproducibility—particularly in controlling the Ce^{3+}/Ce^{4+} ratio, Fe content, and MTX conjugation efficiency—will need to be established to support eventual regulatory approval and translational development.

The study thus establishes a strong foundation for further investigations into the potential of Chit-IOCO-Cy5-MTX as a theranostic nanocomplex for the treatment and diagnosis of atherosclerosis.

CONCLUSION

This study pioneers the use of cerium oxide for atherosclerosis treatment alongside the incorporation of iron oxide for tracking cerium oxide delivery and allowing molecular imaging of atherosclerotic plaques by MRI. The study utilized electrostatic self-assembly to fabricate nanocomplexes composed of chitosan, iron oxide, and cerium oxide, with chitosan serving as a carrier to encapsulate iron oxide and ceria. The nanocomplexes were modified with Cy5 and MTX, with MTX serving as a targeting ligand and an enhancer for treatment. *In vitro* cell MRI and fluorescence imaging suggested that the targeting ability of the nanocomposite on active macrophages was enhanced by MTX conjugation. Additionally, the conjugation of MTX to the nanocomposite significantly enhanced their anti-inflammatory and anti-ROS capabilities in LPS-stimulated macrophages when compared to non-conjugated Chit-IOCO nanocomposite. *In vivo* studies demonstrated that Chit-IOCO-Cy5-MTX administration significantly reduced plaque formation and the overexpression of inflammatory proteins in the $ApoE^{-/-}$ mice, indicating its potential as a therapeutic agent for atherosclerosis. Furthermore, the transverse relaxivity of Chit-IOCO-Cy5-MTX was higher compared to clinical iron oxide contrast agents, and it exhibited strong MRI T_2 contrast ability, enabling the detection of nanoparticle delivery to the atherosclerotic plaque in $ApoE^{-/-}$ mice. These results suggest that Chit-IOCO-Cy5-MTX holds significant potential as an effective theranostic nanomaterial for the diagnosis and treatment of atherosclerosis.

This work is distinct from prior nanoceria reports by integrating three complementary modules into one nanoplatform: (i) cerium oxide for ROS scavenging and anti-inflammatory activity, (ii) iron oxide for MRI detectability of plaques, and (iii) MTX for targeted macrophage uptake. To

https://doi.org/10.1021/acsnanomed.5c00036
ACS Nano Med. 2026, 1, 250−267

our knowledge, this triple-functional design has not been previously reported in atherosclerosis therapy. To enhance translational relevance, it is necessary to conduct a comprehensive study to compare the performance of our newly developed nanomedicine against clinically approved therapeutics such as statins and colchicine under the same experimental conditions. This however will require additional animal ethics approval, time, funding and resources. Nevertheless, our promising results showing an almost complete reduction of atherosclerotic plaques in mice treated with Chit-IOCO-MTX are very encouraging and provide a strong foundation for further studies toward clinical translation.

Previously, we demonstrated that these nanocomplexes exhibit long-lasting and potent anticancer effects.[27] Combined with the findings from this study, we conclude that Chit-IOCO is a highly versatile material with both strong anticancer and cardiovascular-protective properties. This is a significant discovery, as most anticancer drugs carry the risk of cardiotoxicity, whereas Chit-IOCO does not.

■ ASSOCIATED CONTENT

Data Availability Statement

Data will be made available on request.

Supporting Information

The Supporting Information is available free of charge at https://pubs.acs.org/doi/10.1021/acsnanomed.5c00036.

Detailed materials and methods; synthesis and characterization of nanoparticles (TEM, STEM-EDS, DLS, zeta potential, FTIR, XPS); MRI relaxivity measurements; *in vitro* cell viability, hemocompatibility, ROS scavenging, LDL uptake, and Western blot assays; *in vivo* MRI diagnosis and therapeutic studies in ApoE$^{-/-}$ mice; histological, ORO staining, and biochemical analyses; statistical analysis methods; and Figures S1−S12 (PDF)

■ AUTHOR INFORMATION

Corresponding Author

Hang Thu Ta − *School of Environment and Science, Griffith University, Brisbane, Queensland 4111, Australia; Queensland Quantum and Advanced Technologies Research Institute, Griffith University, Brisbane, Queensland 4111, Australia;* orcid.org/0000-0003-1188-0472; Phone: +61 (7) 3735 5384; Email: h.ta@griffith.edu.au

Authors

Yuao Wu − *School of Environment and Science, Griffith University, Brisbane, Queensland 4111, Australia; Queensland Quantum and Advanced Technologies Research Institute, Griffith University, Brisbane, Queensland 4111, Australia*

Huong D. N. Tran − *School of Environment and Science, Griffith University, Brisbane, Queensland 4111, Australia; Australian Institute for Bioengineering and Nanotechnology, University of Queensland, Brisbane, Queensland 4072, Australia*

Dimple Sajin − *School of Environment and Science, Griffith University, Brisbane, Queensland 4111, Australia*

Shehzahdi S. Moonshi − *School of Environment and Science, Griffith University, Brisbane, Queensland 4111, Australia;* orcid.org/0000-0003-2048-595X

Najma Annuria Fithri − *School of Environment and Science, Griffith University, Brisbane, Queensland 4111, Australia; Australian Institute for Bioengineering and Nanotechnology, University of Queensland, Brisbane, Queensland 4072, Australia*

Nyoman Kurniawan − *Australian Institute for Bioengineering and Nanotechnology, University of Queensland, Brisbane, Queensland 4072, Australia; Centre of Advanced Imaging, University of Queensland, Brisbane, Queensland 4072, Australia*

Complete contact information is available at: https://pubs.acs.org/10.1021/acsnanomed.5c00036

Notes

The authors declare no competing financial interest.

■ ACKNOWLEDGMENTS

This work is funded by Australian National Health and Medical Research Council (HTT: APP1037310, APP2002827) and National Heart Foundation of Australia (HTT: 102761). The authors would like to acknowledge the Australian National Fabrication Facility (Queensland Node), ALS Geochemistry, and National Imaging Facility (a National Collaborative Research Infrastructure Strategy capability) at the Centre for Advanced Imaging, the University of Queensland, for access to key items of equipment.

■ ABBREVIATION

Chit = Chitosan
CO = Cerium oxide nanoparticles
COX-2 = Cyclooxygenase-2
CVDs = Cardiovascular diseases
Cy5 = Cyanine-5
EDC = 1-Ethyl-3-(3-dimethylaminopropyl)-1-carbodiimide
IL-6 = Interleukin 6
iNOS = Inducible nitric oxide synthase
IO = Iron oxide nanoparticles
LPS = Lipopolysaccharides
MRI = Magnetic resonance imaging
MTX = Methotrexate
PAA = Poly(acrylic acid)
PBS = Phosphate-buffered saline
PDI = Polydispersity Index
ROS = Reactive oxygen species
SDS = Sodium dodecyl sulfate
TE = Echo time
TEM = Transmission electron microscopy
TNF-α = Tumour necrosis factor-α
TSC = Trisodium citrate
ZP = Zeta potential

■ REFERENCES

(1) Cardiovascular diseases (CVDs). *World Health Organization*. https://www.who.int/news-room/fact-sheets/detail/cardiovascular-diseases-(cvds).

(2) Perera, B.; Wu, Y.; Nguyen, N. T.; Ta, H. T. Advances in drug delivery to atherosclerosis: Investigating the efficiency of different nanomaterials employed for different type of drugs. *Mater. Today Bio* **2023**, *22*, No. 100767.

(3) Akther, F.; Zhang, J.; Tran, H. D. N.; Fallahi, H.; Adelnia, H.; Phan, H. P.; Nguyen, N. T.; Ta, H. T. Atherothrombosis-on-Chip: A Site-Specific Microfluidic Model for Thrombus Formation and Drug Discovery. *Adv. Biol.* **2022**, *6* (7), No. e2101316.

(4) Akther, F.; Fallahi, H.; Zhang, J.; Nguyen, N. T.; Ta, H. T. Evaluating thrombosis risk and patient-specific treatment strategy using an atherothrombosis-on-chip model. *Lab Chip* **2024**, *24* (11), 2927−2943.
(5) Wolf, D.; Ley, K. Immunity and inflammation in atherosclerosis. *Circulation research* **2019**, *124* (2), 315−327.
(6) Zhou, Y.; Little, P. J.; Downey, L.; Afroz, R.; Wu, Y.; Ta, H. T.; Xu, S.; Kamato, D. The role of toll-like receptors in atherothrombotic cardiovascular disease. *ACS Pharmacology & Translational Science* **2020**, *3* (3), 457−471.
(7) Bonomini, F.; Tengattini, S.; Fabiano, A.; Bianchi, R.; Rezzani, R. Atherosclerosis and oxidative stress. *Histol Histopathol* **2008**, *23* (3), 381−390.
(8) Tyrrell, D. J.; Goldstein, D. R. Ageing and atherosclerosis: vascular intrinsic and extrinsic factors and potential role of IL-6. *Nature Reviews Cardiology* **2021**, *18* (1), 58−68.
(9) Cipollone, F.; Fazia, M. L. COX-2 and atherosclerosis. *Journal of Cardiovascular Pharmacology* **2006**, *47*, S26−S36.
(10) Liu, Y.; Wu, Y.; Zhang, R.; Lam, J.; Ng, J. C.; Xu, Z. P.; Li, L.; Ta, H. T. Investigating the use of layered double hydroxide nanoparticles as carriers of metal oxides for theranostics of ROS-related diseases. *ACS Applied Bio Materials* **2019**, *2* (12), 5930−5940.
(11) Bäck, M.; Hansson, G. K. Anti-inflammatory therapies for atherosclerosis. *Nature Reviews Cardiology* **2015**, *12* (4), 199−211.
(12) Wu, Y.; Ta, H. T. Different approaches to synthesising cerium oxide nanoparticles and their corresponding physical characteristics, and ROS scavenging and anti-inflammatory capabilities. *J. Mater. Chem. B* **2021**, *9* (36), 7291−7301.
(13) Wu, Y.; Yang, Y.; Zhao, W.; Xu, Z. P.; Little, P. J.; Whittaker, A. K.; Zhang, R.; Ta, H. T. Novel iron oxide−cerium oxide core−shell nanoparticles as a potential theranostic material for ROS related inflammatory diseases. *J. Mater. Chem. B* **2018**, *6* (30), 4937−4951.
(14) Wu, Y.; Zhang, R.; Tran, H. D.; Kurniawan, N. D.; Moonshi, S. S.; Whittaker, A. K.; Ta, H. T. Chitosan nanococktails containing both ceria and superparamagnetic iron oxide nanoparticles for reactive oxygen species-related theranostics. *ACS Applied Nano Materials* **2021**, *4* (4), 3604−3618.
(15) Wu, Y.; Cowin, G.; Moonshi, S. S.; Tran, H. D.; Fithri, N. A.; Whittaker, A. K.; Zhang, R.; Ta, H. T. Engineering chitosan nano-cocktail containing iron oxide and ceria: a two-in-one approach for treatment of inflammatory diseases and tracking of material delivery. *Materials Science and Engineering: C* **2021**, *131*, No. 112477.
(16) Wang, S.; Zhou, Y.; Liang, X.; Xu, M.; Li, N.; Zhao, K. Platinum-cerium bimetallic nano-raspberry for atherosclerosis treatment via synergistic foam cell inhibition and P2Y12 targeted antiplatelet aggregation. *Chemical Engineering Journal* **2022**, *430*, No. 132859.
(17) Fu, X.; Yu, X.; Jiang, J.; Yang, J.; Chen, L.; Yang, Z.; Yu, C. Small molecule-assisted assembly of multifunctional ceria nanozymes for synergistic treatment of atherosclerosis. *Nat. Commun.* **2022**, *13* (1), 6528.
(18) Zhao, L.; Ma, D.; Wang, L.; Su, X.; Feng, L.; Zhu, L.; Chen, Y.; Hao, Y.; Wang, X.; Feng, J. Metabolic changes with the occurrence of atherosclerotic plaques and the effects of statins. *Frontiers in Immunology* **2023**, *14* (2023), na DOI: 10.3389/fimmu.2023.1301051.
(19) Härdtner, C.; Ehlert, C. A.; Hilgendorf, I. New insights in statins affecting atheromatous plaque macrophages. *Current Opinion in Lipidology* **2021**, *32* (4), 258−264.
(20) Ta, H. T.; Arndt, N.; Wu, Y.; Lim, H. J.; Landeen, S.; Zhang, R.; Kamato, D.; Little, P. J.; Whittaker, A. K.; Xu, Z. P. Activatable magnetic resonance nanosensor as a potential imaging agent for detecting and discriminating thrombosis. *Nanoscale* **2018**, *10* (31), 15103−15115.
(21) Ta, H. T.; Li, Z.; Wu, Y.; Cowin, G.; Zhang, S.; Yago, A.; Whittaker, A. K.; Xu, Z. P. Effects of magnetic field strength and particle aggregation on relaxivity of ultra-small dual contrast iron oxide nanoparticles. *Materials Research Express* **2017**, *4* (11), No. 116105.
(22) Rehman, A. U.; Wu, Y.; Tran, H. D.; Vazquez-Prada, K.; Liu, Y.; Adelnia, H.; Kurniawan, N. D.; Anjum, M. N.; Moonshi, S. S.; Ta, H. T. Silver/iron oxide nano-popcorns for imaging and therapy. *ACS Applied Nano Materials* **2021**, *4* (10), 10136−10147.
(23) Moonshi, S. S.; Wu, Y.; Ta, H. T. Visualizing stem cells in vivo using magnetic resonance imaging. *Wiley Interdiscip Rev. Nanomed Nanobiotechnol* **2022**, *14* (2), No. e1760.
(24) Vazquez-Prada, K. X.; Moonshi, S. S.; Wu, Y.; Akther, F.; Tse, B. W.; Sokolowski, K. A.; Peter, K.; Wang, X.; Xu, G.; Ta, H. T. A Spiky Silver-Iron Oxide Nanoparticle for Highly Efficient Targeted Photothermal Therapy and Multimodal Imaging of Thrombosis. *Small* **2023**, *19*, No. 2205744.
(25) Fithri, N. A.; Wu, Y.; Cowin, G.; Akther, F.; Tran, H. D.N.; Tse, B.; van Holthe, N. W.; Moonshi, S. S.; Peter, K.; Wang, X.; Truong, N. P.; Ta, H. T. Gold-iron oxide nanoparticle: A unique multimodal theranostic approach for thrombosis. *Applied Materials Today* **2023**, *31*, No. 101750.
(26) Vazquez-Prada, K. X.; Moonshi, S. S.; Xu, Z. P.; Ta, H. T. Photothermal nanomaterials for theranostics of atherosclerosis and thrombosis. *Applied Materials Today* **2023**, *35*, 101967.
(27) Tang, J. L.; Moonshi, S. S.; Wu, Y.; Cowin, G.; Vazquez-Prada, K. X.; Tran, H. D.; Bulmer, A. C.; Ta, H. T. A methotrexate labelled dual metal oxide nanocomposite for long-lasting anti-cancer theranostics. *Materials Today Bio* **2025**, *30*, No. 101377.
(28) Brown, P. M.; Pratt, A. G.; Isaacs, J. D. Mechanism of action of methotrexate in rheumatoid arthritis, and the search for biomarkers. *Nat. Rev. Rheumatol* **2016**, *12* (12), 731−742.
(29) Cutolo, M.; Sulli, A.; Pizzorni, C.; Seriolo, B.; Straub, R. H. Anti-inflammatory mechanisms of methotrexate in rheumatoid arthritis. *Annals of the rheumatic diseases* **2001**, *60* (8), 729−735.
(30) Barrett, T. J. Macrophages in atherosclerosis regression. *Arterioscler., Thromb., Vasc. Biol.* **2020**, *40* (1), 20−33.
(31) Kim, H.-J.; Kim, M.-J.; Lee, C.-K.; Hong, Y.-H. Effects of methotrexate on carotid intima-media thickness in patients with rheumatoid arthritis. *Journal of Korean medical science* **2015**, *30* (11), 1589−1596.
(32) Ridker, P. M.; Everett, B. M.; Pradhan, A.; MacFadyen, J. G.; Solomon, D. H.; Zaharris, E.; Mam, V.; Hasan, A.; Rosenberg, Y.; Iturriaga, E.; et al. Low-dose methotrexate for the prevention of atherosclerotic events. *New Engl J. Med.* **2019**, *380* (8), 752−762.
(33) Zia, A.; Wu, Y.; Nguyen, T.; Wang, X.; Peter, K.; Ta, H. T. The choice of targets and ligands for site-specific delivery of nanomedicine to atherosclerosis. *Cardiovascular research* **2020**, *116* (13), 2055−2068.
(34) Yi, Y.-S. Folate receptor-targeted diagnostics and therapeutics for inflammatory diseases. *Immune Network* **2016**, *16* (6), 337−343.
(35) Nakashima-Matsushita, N.; Homma, T.; Yu, S.; Matsuda, T.; Sunahara, N.; Nakamura, T.; Tsukano, M.; Ratnam, M.; Matsuyama, T. Selective expression of folate receptor β and its possible role in methotrexate transport in synovial macrophages from patients with rheumatoid arthritis. *Arthritis & Rheumatism* **1999**, *42* (8), 1609−1616.
(36) Song, L.; Pan, Z.; Zhang, H.; Li, Y.; Zhang, Y.; Lin, J.; Su, G.; Ye, S.; Xie, L.; Li, Y.; Hou, Z. Dually folate/CD44 receptor-targeted self-assembled hyaluronic acid nanoparticles for dual-drug delivery and combination cancer therapy. *J. Mater. Chem. B* **2017**, *5* (33), 6835−6846.
(37) Xie, J.; Fan, Z.; Li, Y.; Zhang, Y.; Yu, F.; Su, G.; Xie, L.; Hou, Z. Design of pH-sensitive methotrexate prodrug-targeted curcumin nanoparticles for efficient dual-drug delivery and combination cancer therapy. *International journal of nanomedicine* **2018**, *13*, 1381−1398.
(38) Wu, Y.; Zhang, R.; Tran, H. D. N.; Kurniawan, N. D.; Moonshi, S. S.; Whittaker, A. K.; Ta, H. T. Chitosan Nanococktails Containing Both Ceria and Superparamagnetic Iron Oxide Nanoparticles for Reactive Oxygen Species-Related Theranostics. *ACS Applied Nano Materials* **2021**, *4* (4), 3604−3618.
(39) Wong, P. T.; Choi, S. K. Mechanisms and Implications of Dual-Acting Methotrexate in Folate-Targeted Nanotherapeutic Delivery.

International Journal of Molecular Sciences [Online] **2015**, *16*, 1772−1790.
(40) Nakagawa, H.; Maeda, S. Inflammation-and stress-related signaling pathways in hepatocarcinogenesis. *World journal of gastroenterology* **2012**, *18* (31), 4071.
(41) Brasier, A. R. The nuclear factor-κB−interleukin-6 signalling pathway mediating vascular inflammation. *Cardiovascular research* **2010**, *86* (2), 211−218.
(42) Lahti, A.; Jalonen, U.; Kankaanranta, H.; Moilanen, E. c-Jun NH2-terminal kinase inhibitor anthra (1, 9-cd) pyrazol-6 (2H)-one reduces inducible nitric-oxide synthase expression by destabilizing mRNA in activated macrophages. *Molecular pharmacology* **2003**, *64* (2), 308−315.
(43) Cho, W.; Choe, J. Prostaglandin E2 stimulates COX-2 expression via mitogen-activated protein kinase p38 but not ERK in human follicular dendritic cell-like cells. *BMC immunology* **2020**, *21*, 1−8.
(44) Getz, G. S.; Reardon, C. A. Animal models of atherosclerosis. *Arterioscler., Thromb., Vasc. Biol.* **2012**, *32* (5), 1104−1115.
(45) Singh, Z.; Karthigesu, I. P.; Singh, P.; Rupinder, K. Use of malondialdehyde as a biomarker for assessing oxidative stress in different disease pathologies: a review. *Iranian Journal of Public Health* **2014**, *43*, 7−16.
(46) Ta, H. T.; Dass, C. R.; Larson, I.; Choong, P. F.; Dunstan, D. E. A chitosan hydrogel delivery system for osteosarcoma gene therapy with pigment epithelium-derived factor combined with chemotherapy. *Biomaterials* **2009**, *30* (27), 4815−23.
(47) Li, C.; Luo, X.; Qian, C.; Huang, J.; Yi, X.; Su, H.; Han, Y. Folate receptor-mediated targeted therapy for rheumatoid arthritis by methotrexate-phospholipid complex nano-emulsions. *J. Drug Targeting* **2023**, *31* (4), 402−410.
(48) Garcia, G. E.; Lu, Y. J.; Truong, L. D.; Roncal-Jiménez, C. A.; Miyazaki, M.; Miyazaki-Anzai, S.; Cara-Fuentes, G.; Andres-Hernando, A.; Lanaspa, M.; Johnson, R. J.; Leamon, C. P. A Novel Treatment for Glomerular Disease: Targeting the Activated Macrophage Folate Receptor with a Trojan Horse Therapy in Rats. *Cells* **2021**, *10* (8), 2113.
(49) Muller, I. B.; Lin, M.; Jonge, R. d.; Will, N.; López-Navarro, B.; Laken, C. v. d.; Struys, E. A.; Oudejans, C. B. M.; Assaraf, Y. G.; Cloos, J.; Puig-Kröger, A.; Jansen, G. Methotrexate Provokes Disparate Folate Metabolism Gene Expression and Alternative Splicing in Ex Vivo Monocytes and GM-CSF- and M-CSF-Polarized Macrophages. *International Journal of Molecular Sciences* **2023**, *24* (11), 9641.
(50) Ridker, P. M; Everett, B. M.; Pradhan, A.; MacFadyen, J. G.; Solomon, D. H.; Zaharris, E.; Mam, V.; Hasan, A.; Rosenberg, Y.; Iturriaga, E.; Gupta, M.; Tsigoulis, M.; Verma, S.; Clearfield, M.; Libby, P.; Goldhaber, S. Z.; Seagle, R.; Ofori, C.; Saklayen, M.; Butman, S.; Singh, N.; Le May, M.; Bertrand, O.; Johnston, J.; Paynter, N. P.; Glynn, R. J. Low-Dose Methotrexate for the Prevention of Atherosclerotic Events. *New Engl J. Med.* **2019**, *380* (8), 752−762.
(51) Tang, J. L. Y.; Moonshi, S. S.; Ta, H. T. Nanoceria: an innovative strategy for cancer treatment. *Cell. Mol. Life Sci.* **2023**, *80* (2), 46.
(52) Tang, J. L. Y.; Moonshi, S. S.; Wu, Y.; Cowin, G.; Vazquez-Prada, K. X.; Tran, H. D. N.; Bulmer, A. C.; Ta, H. T. A methotrexate labelled dual metal oxide nanocomposite for long-lasting anti-cancer theranostics. *Materials Today Bio* **2025**, *30*, No. 101377.
(53) Ma, H.; Liu, Z.; Koshy, P.; Sorrell, C. C.; Hart, J. N. Density Functional Theory Investigation of the Biocatalytic Mechanisms of pH-Driven Biomimetic Behavior in CeO2. *ACS Appl. Mater. Interfaces* **2022**, *14* (9), 11937−11949.
(54) Park, G.; Lee, S. H.; Han, J.-Y.; Oh, D.-S. Altered TNF-α response by Aconibal® and methotrexate in a lipopolysaccharide-induced setting of inflammatory conditions: Potential on a synergistic combination. *Journal of Ethnopharmacology* **2018**, *213*, 191−197.
(55) Ban, D.; Yu, H.; Xiang, Z.; Li, C.; Yu, P.; Wang, J.; Liu, Y. Cerium oxide nanoparticles alleviate neuropathic pain by modulating macrophage polarization in a rat SCI model. *Journal of Pain Research* **2022**, *15*, 3369−3380.
(56) Selvaraj, V.; Manne, N. D.; Arvapalli, R.; Rice, K. M.; Nandyala, G.; Fankenhanel, E.; Blough, E. R. Effect of cerium oxide nanoparticles on sepsis induced mortality and NF-κB signaling in cultured macrophages. *Nanomedicine* **2015**, *10* (8), 1275−1288.
(57) Chen, H.; Howatt, D. A.; Franklin, M. K.; Amioka, N.; Sawada, H.; Daugherty, A.; Lu, H. S. A mini-review on quantification of atherosclerosis in hypercholesterolemic mice. *Global translational medicine* **2022**, *1* (1), 1.
(58) Amirbekian, S.; Long, R. C., Jr; Consolini, M. A.; Suo, J.; Willett, N. J.; Fielden, S. W.; Giddens, D. P.; Taylor, W. R.; Oshinski, J. N. In vivo assessment of blood flow patterns in abdominal aorta of mice with MRI: implications for AAA localization. *American Journal of Physiology-Heart and Circulatory Physiology* **2009**, *297* (4), H1290−H1295.
(59) Stigliano, C.; Ramirez, M. R.; Singh, J. V.; Aryal, S.; Key, J.; Blanco, E.; Decuzzi, P. Methotraxate-Loaded Hybrid Nanoconstructs Target Vascular Lesions and Inhibit Atherosclerosis Progression in ApoE−/− Mice. *Adv. Healthcare Mater.* **2017**, *6* (13), No. 1601286.
(60) Di Francesco, V.; Gurgone, D.; Palomba, R.; Ferreira, M. F. M. M.; Catelani, T.; Cervadoro, A.; Maffia, P.; Decuzzi, P. Modulating Lipoprotein Transcellular Transport and Atherosclerotic Plaque Formation in ApoE−/−Mice via Nanoformulated Lipid−Methotrexate Conjugates. *ACS Appl. Mater. Interfaces* **2020**, *12* (34), 37943−37956.
(61) Wen, Y.; Chen, L.; Zhou, L.; Leng, F.; Yang, Z.; Yu, C. Bionic receptor for atherosclerosis therapy: Molecularly imprinted polymers mediate unique cholesterol efflux and inhibit inflammation. *Chemical Engineering Journal* **2022**, *430*, No. 132870.
(62) Duan, H.; Tang, S.-Y.; Goda, K.; Li, M. Enhancing the sensitivity and stability of electrochemical aptamer-based sensors by AuNPs@MXene nanocomposite for continuous monitoring of biomarkers. *Biosens. Bioelectron.* **2024**, *246*, No. 115918.
(63) Jia, J.; Kwon, S.-R.; Baek, S.; Sundaresan, V.; Cao, T.; Cutri, A. R.; Fu, K.; Roberts, B.; Shrout, J. D.; Bohn, P. W. Actively Controllable Solid-Phase Microextraction in a Hierarchically Organized Block Copolymer-Nanopore Electrode Array Sensor for Charge-Selective Detection of Bacterial Metabolites. *Anal. Chem.* **2021**, *93* (43), 14481−14488.
(64) Sun, Y.; Li, M.; Zheng, M.; Zou, Y.; Shi, B. Blood-brain barrier penetrating nanosystems enable synergistic therapy of glioblastoma. *Nano Today* **2024**, *56*, No. 102310.
(65) Golusda, L.; Kuhl, A. A.; Lehmann, M.; Dahlke, K.; Mueller, S.; Boehm-Sturm, P.; Saatz, J.; Traub, H.; Schnorr, J.; Freise, C.; Taupitz, M.; Biskup, K.; Blanchard, V.; Klein, O.; Sack, I.; Siegmund, B.; Paclik, D. Visualization of inflammation in experimental colitis by magnetic resonance imaging using very small superparamagnetic iron oxide particles. *Frontiers in physiology* **2022**, *13*, 1369.
(66) Moonshi, S. S.; Vazquez-Prada, K. X.; Tang, J.; Westra van Holthe, N. J.; Cowin, G.; Wu, Y.; Tran, H. D.; Mckinnon, R.; Bulmer, A. C.; Ta, H. T. Spiky Silver−Iron Oxide Nanohybrid for Effective Dual-Imaging and Synergistic Thermo-Chemotherapy. *ACS Appl. Mater. Interfaces* **2023**, *15*, 42153.
(67) van Zandwijk, J. K.; Simonis, F. F.; Heslinga, F. G.; Hofmeijer, E. I.; Geelkerken, R. H.; Ten Haken, B. Comparing the signal enhancement of a gadolinium based and an iron-oxide based contrast agent in low-field MRI. *PLoS One* **2021**, *16* (8), No. e0256252.
(68) Segers, F. M E; Ruder, A. V; Westra, M. M; Lammers, T.; Dadfar, S. M.; Roemhild, K.; Lam, T. S.; Kooi, M. E.; Cleutjens, K. B J M; Verheyen, F. K; Schurink, G. W H; Haenen, G. R; van Berkel, T. J C; Bot, I.; Halvorsen, B.; Sluimer, J. C; Biessen, E. A L MRI Contrast-enhancement with superparamagnetic iron oxide nanoparticles amplify macrophage foam cell apoptosis in human and murine atherosclerosis. *Cardiovasc. Res.* **2023**, *118*, 3346.
(69) Chen, X.; Li, X.; Chen, Q. Experimental Study of Ultrafine Superparamagnetic Iron Oxide-Enhanced MRI in an Atherosclerotic Plaque Model. *J. Nanosci. Nanotechnol.* **2020**, *20* (12), 7444−7450.

https://doi.org/10.1021/acsnanomed.5c00036
ACS Nano Med. 2026, 1, 250−267

(70) Korchinski, D. J.; Taha, M.; Yang, R.; Nathoo, N.; Dunn, J. F. Iron oxide as an MRI contrast agent for cell tracking: Supplementary Issue. *Magnetic resonance insights* **2015**, *8*, No. S23557.

https://doi.org/10.1021/acsnanomed.5c00036
ACS Nano Med. 2026, 1, 250−267

Supporting information for

Vascular-protective effects of cerium oxide nanoparticles complexed with iron oxide and methotrexate: Reversing atherosclerosis in a murine model

Yuao Wu[1,2], Huong D.N. Tran[1,3], Dimple Sajin[1], Shehzahdi S. Moonshi[1], Najma Annuria Fithri[1,3], Nyoman Kurniawan[3,4], Hang Thu Ta[1,2]*

[1] School of Environment and Science, Griffith University, Brisbane, Queensland 4111, Australia
[2] Queensland Quantum and Advanced Technologies Research Institute, Griffith University, Brisbane, Queensland 4111, Australia
[3] Australian Institute for Bioengineering and Nanotechnology, University of Queensland, Brisbane, Queensland 4072, Australia
[4] Centre of Advanced Imaging, University of Queensland, Brisbane, Queensland 4072, Australia

Corresponding author:
Hang Thu Ta, BEng, MSc, PhD
Professor, School of Environment and Science, and Queensland Micro- and Nanotechnology, Griffith University, Nathan Campus, Brisbane QLD 4111, Australia
Australian Research Council Future Fellow
Australian Heart Foundation Future Leader Fellow
Office: +61 (7) 3735 5384
Email:
h.ta@griffith.edu.au
Website:
https://hangta.group/
https://experts.griffith.edu.au/27034-hang-ta

DETAILED MATERIALS AND METHODS

Ammonium hydroxide solution, sodium chloride, sodium fluoride, Iron (II) ammonium sulfate, cerium nitrate hexahydrate, ethylenediaminetetraacetic acid (EDTA), hydrochloric acid (reagent grade, 37%), ammonium cerium nitrate, sodium acetate trihydrate, low molecular weight chitosan, sodium pyrophosphate decahydratem, sodium orthovanadate, acetic acid, poly(acrylic acid) (PAA), lipopolysaccharides (LPS), Tris base, sodium dodecyl sulfate (SDS), Triton X-100, MES free acid powder and Oil Red O were purchased from Sigma-Aldrich. Trisodium citrate (TSC) was purchased from Chem-supply. Virgin olive oil and fat free instant skim milk powder were purchased from local market Coles. Phosphate-buffered saline (PBS) and Dulbecco's Modified Eagle Medium (DMEM) and Bovine serum albumin (BSA) was purchased from ThermoFisher Scientific. Tetramethyl ethylenediamine, Precision Plus Protein™ Kaleidoscope™ Prestained Protein Standards, ammonium persulfate and 30% Acrylamide/Bis Solution were purchased from Bio Rad. Anti-mouse β-actin (ab8226), anti-mouse COX-2 (ab188183), anti-mouse IL-6 (ab208113), anti-mouse iNOS (ab205529) and anti-mouse TNF-α (ab34674), were purchased from Abcam. To prepare MES buffer, 19.2 g of MES free acid powder was dissolved in distilled water to total volume of 100 ml, and the solution pH was adjusted to 5 using 1N NaOH. UV free 96-well plates were purchased from Greiner Bio-One GmbH (Germany).

Synthesis of the nanocomplexs

Synthesis of iron oxide nanoparticles

Poly(acrylic acid) coated iron oxide (IO-PAA) nanoparticles were generated using a coprecipitation approach.[1] Initially, PAA (200 mg) was dissolved in Milli-Q water (50 mL) and subjected to nitrogen purging for half an hour. This solution was then brought to a refluxing state at 130 °C using an oil bath. A mixture of 0.51 mM $FeCl_3 \cdot 6H_2O$ (0.1378 g) and 0.25 mM $(NH_4)_2Fe(SO_4)_2 \cdot 6H_2O$ (0.099 g) were dissolved in concentrated HCl (1 mL, 37%). This mixture was rapidly added to the heated PAA solution, followed by stirring for a duration of 5 minutes. Next, ammonia solution (15 mL, 30%) was introduced, and the mixture was refluxed for an additional two hours. Afterward, the solution was condensed using an Amicon filter (Millipore, Inc.) with a 50 kDa molecular weight cut-off. The concentrated solution underwent further dialysis against water (5 L) at pH 10 for one day, followed by pH 7 for three days, resulting in the collection of PAA-coated iron oxide nanoparticles, which were stored at 4 °C.

Synthesis of cerium oxide nanoparticles

Cerium oxide nanoparticles were generated using the precipitation technique.[1] $(NH_4)_2Ce(NO_3)_6$ (0.685 g) and CH_3COONa (2.5 g) were prepared in 17.5 ml of deionized water. Following this, CH_3COOH (2.5 mL) was added and stirred at room temperature for 60 minutes. The above solution was subsequently heated at 100 °C with condensation reflux for two hours, forming yellow precipitates. The yellow precipitates were collected by centrifugation at 6000g and rinsed once with deionized water. The precipitates were then redispersed in Milli-Q H2O (5 mL).

Trisodium citrate dihydrate (TSC)-coated cerium oxide nanoparticles (CO-TSC) were prepared by mixing 100 mg of cerium oxide nanoparticles with 0.1 M TSC in Milli-Q H_2O (15 mL) over a period of 24 hours. This solution was stirred, and large agglomerates were eliminated by centrifugation using a 100 kDa molecular weight cut-off Amicon filter (Millipore, Inc.) at 10,000g for 60 seconds. The CO-TSC nanoparticles were stored in a 0.1 M TSC solution and further dialyzed against water employing a SnakeSkin tube (10 kDa MWCO) before use.

Synthesis of Chit-IOCO nanoparticles

The ionic gelation technique was utilized to fabricate Chit-IOCO nanoparticles, wherein IO-PAA and CO-TSC functioned as cross-linkers. The process started with CO-TSC undergoing dialysis in 1 L of Milli-Q water for 30 minutes at room temperature. Then, a combined solution of IO-PAA and CO-TSC (0.5 mL) was pumped into a 4.5 mL solution of chitosan (pH 4.8) at an infusion rate of 0.2 mL/min. This composite solution was then subjected to centrifugation at 11,000 g under 4°C for 30 minutes and sonication for a cumulative time of 2.5 minutes on ice at 50% amplitude, with 30 seconds of active sonication and 30 seconds off.

The iron and cerium concentrations were subsequently quantified by inductively coupled plasma optical emission spectrometry (ICP-OES) by Australia Laboratory Services Brisbane.

Synthesis of Chit-IOCO-Cy5 nanoparticle and Chit-IOCO-Cy5-MTX nanoparticle

To conjugate MTX and Cy5 dye to the chitosan nanoparticles, an EDC-mediated reaction was deployed to facilitate amide bond formation between the amino groups of chitosan (-NH_2) and the carboxyl groups (-COOH) of either methotrexate (MTX) or Cy5-COOH. EDC was instrumental in activating the -COOH functional groups for this process.

Firstly, a mixture of Chit-IOCO (11.96 g, 4.14 μmol), EDC (0.85 mg, 4.43 μmol), and MTX (1.35 mg, 2.98 μmol) in pH 4.8 MilliQ water (9 mL) was prepared and stirred for two hours at room temperature. Subsequently, Cy5-COOH (0.051 mg, 0.098 μmol) was pre-activated with EDC (0.188 mg, 0.98 μmol) in 1 mL of 0.1 M MES buffer at pH 5 for 15 minutes on a shaker, then added into the mixture, and stirred overnight at room temperature. For Chit-IOCO-Cy5, MTX was substituted with MilliQ water at pH 4.8. The resultant mixture was centrifuged at 11,000 g under 4°C for 30 minutes. The pellet was re-dispersed in 1 mL of pH 4.8 water and sonicated for a cumulative time of 2.5 minutes on ice at 30% amplitude, with 20 seconds of active sonication and 20 seconds off. at 30% amplitude for 2 minutes, with an operation mode of 2 seconds ON and 2 seconds OFF, while cooling on ice. The supernatant from the Chit-IOCO-MTX-Cy5 synthesis was subjected to absorbance measurement at 292 nm to determine the conjugation yield of MTX, employing the supernatant from the Chit-IOCO-Cy5 synthesis as a blank control. The quantity of unconjugated MTX was estimated based on the MTX standard curve. The encapsulation efficiency (EE %) of MTX was assessed

using relevant formulas:

$$MTX\ EE\ (wt\ \%) = \frac{weight\ of\ MTX\ in\ reaction - \text{weight of MTX in supernatant}}{weight\ of\ MTX\ in\ reaction} \times 100 \qquad \text{S(1)}$$

Characterisations of the nanoparticles

Transmission Electron Microscopy (TEM) was acquired utilizing a JEOL-JEM-1010 transmission electron microscope, operating at an acceleration voltage of 120 kV. For the imaging process, samples were allocated onto copper grids and were exposed to a staining solution of phosphotungstic acid (10 mg/mL) for a brief period of 30 seconds to increase the visibility of chitosan. The superfluous acid solution was then meticulously eliminated using Kimwipes tissues. Furthermore, parameters such as hydrodynamic size, size distribution, and zeta potential (ZP) of the nanoparticles were assessed using an Anton Paar Litesizer 500 analyzer (Graz, Austria).

MRI

MRI scans were performed using a Bruker 9.4 Tesla preclinical MRI scanner (BioSpec 94/30 USR, Bruker BioSpin MRI, Germany) with Paravision 6.0.1 at the Centre for Advanced Imaging, The University of Queensland. T_2-relaxation times were measured for Chit-IOCO nanoparticles (with Fe concentrations of 0, 0.07, 0.14, 0.7, 1.4, and 2.8 mM), along with Chit-IOCO-Cy5 and Chit-IOCO-Cy5-MTX nanoparticles (with Fe concentrations of 0, 0.05, 0.10, 0.21, 0.42, and 0.85 mM). T_2 values from these samples were collected via a 2D multi-slice multi-echo (MSME) sequence using a repetition time (TR) of 2630 ms, 32 echoes spanning 5–160 ms, 0.117 × 0.117 mm in-plane resolution, bandwidth of 100 kHz, and slice thickness of 2 mm. T_2^* relaxation times were obtained using a multi-gradient-echo (MGE) sequence, with TR = 300 ms, flip angle of 30 degree, 16 echoes within the 3–48 ms range, 0.156 × 0.156 mm in-plane resolution, bandwidth of 100 kHz, and slice thickness of 2 mm. T_2 and T_2* relaxation times were calculated by fitting the MR image intensities at various TEs with an exponential T_2 decay equation using Paravision. Subsequently, T_2 relaxivity (r_2) of each of the nanoparticle was calculated from the slope of a linear regression, which plotted the nanoparticle relaxation rates ($1/T_2$) against its Fe concentrations.

Cell Culture

The RAW 264.7 macrophage cell line, sourced from the American Type Culture Collection (ATCC), was cultured in a non-treated 100 x 20 mm cell culture dish. The cell culture medium consisted of Dulbecco's Modified Eagle Medium (DMEM) supplemented with 10% fetal calf serum, penicillin at a concentration of 100 U/ml, and 1% L-glutamine. Cells were incubated at a temperature of 37 °C under a 5% CO_2 atmosphere.

In vitro cell MRI and fluorescence imaging

The RAW 264.7 cells were cultured in a 6-well plate at a seeding density of 200,000 cells per well for a duration of 24 hours. These cells were then subjected to LPS treatment with either Chit-IOCO-Cy5 or Chit-IOCO-Cy5-MTX, using cerium concentrations ranging from 0 to 2.5 μg/mL for an additional 24 hours. After this treatment, the cells were isolated and centrifuged at a speed of 200 g for a period of 5 minutes. The isolated cells were subsequently resuspended in 200 μL of 1% low-gelling temperature agarose. From this suspension, 50 μL was quickly transferred into a pre-constructed phantom tube, prepared based on a previously published method[2]. The T_2^* relaxation times was determined using the same method above. Fluorescence images of the cells were acquired using an Azure Sapphire Biomolecular Imager, set at an intensity of 1. Fluorescent intensity was quantified using ImageJ, with the fluorescence of the 0 mg/mL sample set as control for comparison.

Biocompatibility of Chit-IOCO, Chit-IOCO-Cy5, Chit-IOCO-Cy5-MTX nanoparticles, MTX - cytotoxicity study

Once the RAW 264.7 cells reached around 85% confluence, they were gently detached using 2 mL of chilled 1 × PBS and then dispensed into a 96-well plate with a density of 10,000 cells per well. Following a 24-hour incubation period, cells were subjected to treatment with different Chit-IOCO, Chit-IOCO-Cy5, and Chit-IOCO-Cy5-MTX, with Ce concentrations ranging from 0 to 10.0 μg/mL. In parallel, free MTX was also tested at concentrations spanning 0 to 7.58 μg/mL. After treatment, the RAW 264.7 cells were wash with 1x PBS once and subsequently incubated with 1× PrestoBlue cell viability reagent for half an hour, with the intention of evaluating their proliferation and viability through the analysis of fluorescence intensity. Fluorescence intensity was measured using a BMG LABTECH FLUOstar Omega plate reader, with excitation and emission wavelengths set at 560 nm and 590 nm, respectively. The fluorescence intensity of the 0 mg/mL sample was designated as indicative of 100% cell viability.

Haemocompatibility of Chit-IOCO, Chit-IOCO-Cy5, Chit-IOCO-Cy5-MTX nanoparticles, MTX

Human whole blood was obtained from Australian Red Cross Blood Service under a human ethics approved by Griffith University Human Ethics Committee (approval number: 2021/598). A volume of 270 μl of whole blood was subjected to treatment with 30 μl of nanoparticles (Chit-IOCO, Chit-IOCO-Cy5, Chit-IOCO-Cy5-MTX) with different Ce concentrations, and free MTX, with pH maintained at 7.4. Control groups were also included, with one treated with 1% Triton X-100 (positive control), and another with PBS (negative control). Following one hour incubation at 37°C, the mixed solution was centrifuged at 14,000 g for a duration of 20 minutes, after which the supernatant was carefully collected for subsequent analysis. Absorbance was then measured at a wavelength of 545 nm, employing the BMG LABTECH FLUOstar Omega, images was captured using an iPhone.

$$\text{Hemolysis ratio (\%)} = \frac{A_{sample} - A_{negative\ control}}{A_{positive\ control} - A_{negative\ control}} \times 100\% \quad \text{S(2)}$$

Where:

- A_{sample} is the absorbance of the sample-treated red blood cell suspension,
- $A_{negative\ control}$ is the absorbance of the red blood cells in isotonic saline (0% hemolysis),
- $A_{positive\ control}$ is the absorbance of the red blood cells in distilled water (100% hemolysis).

The hemocompatibility percentage was then calculated as:

$$\text{Hemocompatibility (\%)} = 100\ \% - \text{Hemolysis ratio (\%)} \quad \text{S(3)}$$

***In Vitro* ROS Scavenging and LDL uptake Cell-Based Assay**

DCF-DA was used to detect ROS level. DCF-DA (2',7'-dichlorodihydrofluorescein diacetate) serves as a fluorescent probe for assessing reactive oxygen species (ROS) within cells, transitioning from non-fluorescent to highly fluorescent upon ROS interaction. Initially non-fluorescent, DCF-DA is converted to DCFH (2',7'-dichlorodihydrofluorescein) by cellular esterases and, upon encountering ROS, is oxidized to DCF (2',7'-dichlorofluorescein), yielding a fluorescence that quantitatively reflects oxidative stress levels.

The RAW 264.7 cells were cultured in a 96-well plate at a seeding density of 10,000 cells per well for a duration of 24 hours. These cells were then subjected to LPS treatment with either Chit-IOCO-Cy5 or Chit-IOCO-Cy5-MTX, using cerium concentrations ranging from 0 to 2.5 μg/mL, as well as free MTX at concentrations ranging from 0 to 3.79 μg/mL. After 24-hour incubation, cell was washed with 1x PBS once and then treated with 25 μM DCF-DA for 10 minutes in a 37 °C and 5% CO_2. DCF-DA was then replaced by 1x PBS for the subsequent ROS detection. The fluorescence intensity was measured using a BMG LABTECH FLUOstar Omega, which employed an excitation wavelength of 485 nm and an emission wavelength of 590 nm. For the capture of both brightfield and fluorescence images, an fluorescence microscope (CKX53, Olympus) equipped with a digital camera (DP74, Olympus) was utilized.

RAW 264.7 macrophages were seeded in 24-well plates at a density of 5×10^4 cells/well and incubated for 24 h. Cells were then divided into four groups (n = 5 wells per group): (i) Cell control, (ii) LPS (1 μg/mL), (iii) LPS + Chit-IOCO, and (iv) LPS + Chit-IOCO-Cy5-MTX. Nanoparticles were added at a final cerium concentration of 0.25 μg/mL in 500 μL medium per well. Cells were incubated with LPS and the respective treatments for 24 h. Subsequently, the medium was replaced with 40 μg/mL ox-LDL in fresh medium for 4 h. Cells were washed three times with PBS and stained with Oil Red O to evaluate lipid accumulation. A 0.5% Oil Red O stock solution in

100% isopropanol was diluted with distilled water at a 6:4 ratio, equilibrated for 10 min at room temperature, and filtered through a 0.22 μm syringe filter. A total of 250 μL of working solution was added to each well and incubated for 15 min. After staining, cells were washed twice with 78% methanol and rinsed with distilled water. Foam cells were identified by the presence of cytoplasmic lipid droplets stained with Oil Red O. The total number of cells was quantified using ImageJ particle counting, Oil Red O–positive foam cells were counted manually under a microscope. The percentage of foam cells was calculated as the ratio of Oil Red O–positive cells to the total number of cells.

Western blot analysis for *in vitro* assay

The RAW 264.7 cells were cultured in a 6-well plate at a seeding density of 200,000 cells per well for a duration of 24 hours. The cells then underwent individual treatments with either cell culture medium (control), 1 μg/ml of LPS (stimulation), or 1 μg/mL of LPS combined with different nanomaterials or MTX at various concentrations (treatment) for another 24 hours. Following the treatment, the cells were lysed and spun down, the supernatant was analysed to identify protein concentration via the micro BCA assay kit. For each sample, approximately 30 μg of protein was mixed with 5× protein loading buffer, denatured (95°C for 5 mins), and introduced into a 12.5% SDS-PAGE gel. The proteins will be electrophoretically separated by initially running the SDS-PAGE gel at 80V for 15 minutes, followed by an increased voltage of 120V for an additional 50 minutes. These proteins were then transferred to a Mini LF PVDF membrane and subjected to triple wash cycles with 1× TBST (20 mM Tris, 150 mM NaCl, 0.1% (w/v) Tween® 20 detergent), each lasting 5 minutes. Subsequently, the membrane underwent blocking with 5% light milk in 1xTBST for 60 minutes and overnight incubation with primary antibodies targeting IL-6, TNF-α, COX-2, iNOS, or β-actin in a 4 °C with rocking. After incubation, the membranes were washed thrice with 1× TBST for 5 minutes and exposed to secondary anti-rabbit HRP antibodies at room temperature for an hour with rocking. Once each target protein's image was taken, the PVDF membranes were subjected to three cycles of treatment with stripping buffer (20 mM Glycine, 1% SDS, in H_2O, pH 2.0 by HCl) for 10 minutes to remove any remaining antibodies on the membrane. The membranes were then re-blocked using the previously described method. Chemiluminescent images of the LF PVDF membrane were captured with the Azure Sapphire Biomolecular Imager, and the gray values of chemiluminescence bands were scrutinized using ImageJ.

Animal study

The animal experiment was conducted at the University of Queensland, Brisbane, Australia. It was performed under the ethics approval number AIBN/CAI/133/20. We strictly followed national guidelines for the care and handling of laboratory animals. Additionally, the experiment received approval from the University of Queensland's animal care and ethics committees and complied with the European Parliament Directive 2010/63/EU guidelines. The animals were maintained under a balanced 12-hour light/dark cycle, with free access to both food and water. We utilized 8-week-old male $ApoE^{-/-}$ and C57BL/6 mice (sourced from the Animal Resources Centre, ARC,

Western Australia), who were put on a high-fat diet (Specialty Feeds, composed of 23% fat and 0.19% cholesterol, SF03-020) for a period ranging between 7 to 9 weeks. For in vivo MRI study, mice have been treated with high-fat diet for 9 weeks before pre-injection MRI scans. For in vivo treatment study, mice have been treated with high-fat diet for 7 weeks before the IV injection of the nanoparticles. As a control, 8-week-old C57BL/6 mice were kept on a normal diet.

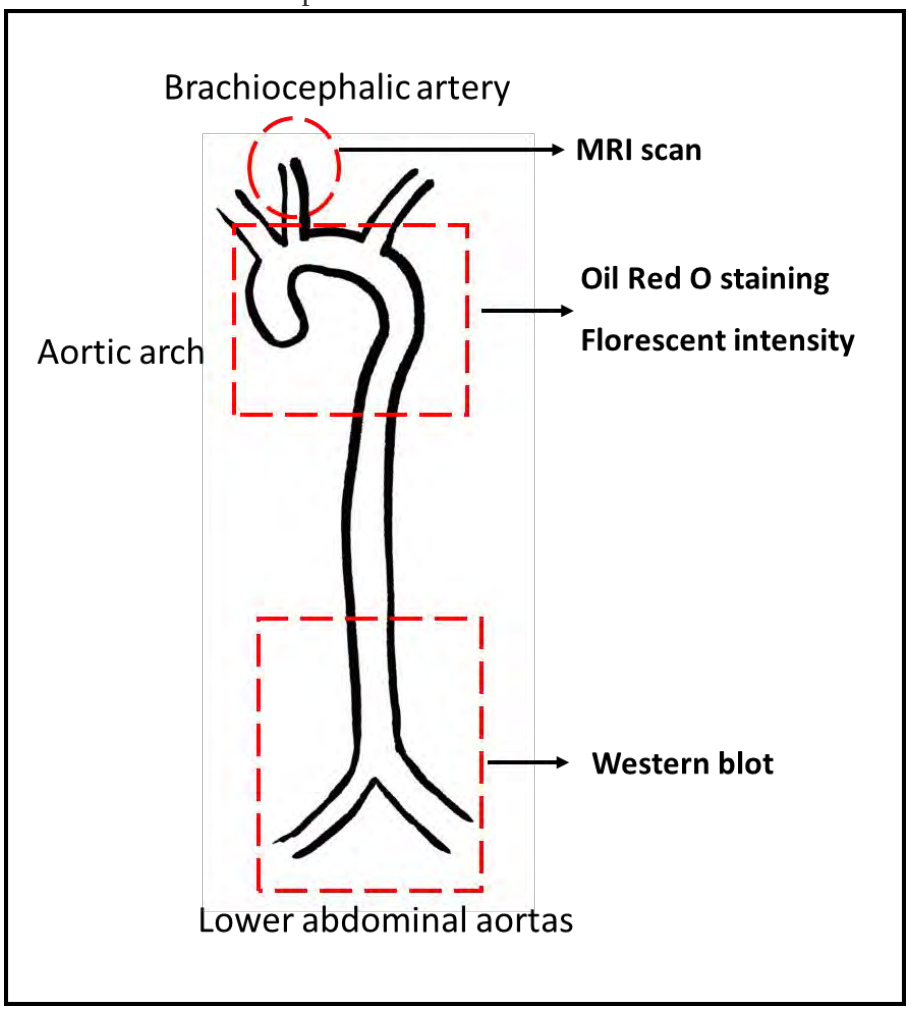

Scheme S1. Localization of Tests in Different Segments of Mice Aorta: Aortic Arch, Lower Abdominal Aorta, and Brachiocephalic Artery. Oil Red O staining and fluorescent tests were conducted in the aortic arch segment, while MRI scans were localized at the brachiocephalic artery above the aortic arch. The lower abdominal aortas were collected for the western blot test.

***In vivo* diagnosis using MRI**

Before contrast agent injection, pre-injection MRI scans were performed to obtain a baseline. Subsequently, saline, Chit-IOCO-Cy5 (containing 0.17 mg Ce/kg of mouse), and Chit-IOCO-Cy5-MTX (containing 0.17 mg/kg of cerium and 1 mg/kg of MTX) were intravenously injected as a single dose after 9 weeks of high fat diet treatment. The post-injection MRI scans were performed one day after injection.

MRI data were acquired (Scheme 2) using Bruker 9.4 T at the Centre for Advanced Imaging. We employed a carefully monitored and humane approach for imaging of

mice. The mice were anesthetized using 2% isoflurane (Forane), with continuous monitoring of their body temperature (rectal thermometry), respiratory rate (acoustic sensor) and heart rate (pulse oximetry) to ensure their well-being. A heating mat was also employed to maintain a stable body temperature throughout the MRI scanning process. The duration of the MRI scans was kept to about one hour, optimizing both efficiency and animal comfort. Following the pre-injection scan, mice were intravenously injected with saline or the nanocomplex and then fully recovered on the heating mat. The conditions for the post-injection scan mirrored those of the pre-injection scan to maintain consistency in the procedure. Following the completion of the post-injection scan, the mice were humanely euthanized using cervical dislocation while under anesthetized with 2% isoflurane (Forane) administered via inhalation, ensuring minimal distress to the animals. . Heart and aorta images were acquired using a retrospective gating INTRAGATE sequence (ref). The INTRAGATE sequence separated MR images into several cardiac phases, to allow high resolution visualisation of the aorta with minimal motion artefacts. The following images were acquired:
Localiser images: TR = 11 ms, TE = 2 ms, field of view 20 × 16 mm, slice thickness = 1 mm, matrix = 250 × 200, flip angle = 10°, bandwidth = 100kHz.
A pair of INTRAGATE images acquired with short and long TEs: TR = 17 ms, TE = 2 ms (short TE) and 6 ms (long TE), field of view 20 × 16 mm, slice thickness = 1 mm, matrix = 250 × 200, flip angle = 10°, bandwidth = 100kHz. The short TE produced proton density (PD) weighted images, whereas the long TE produced T_2^*-weighted images.

MRI (PD/T_2^*) intensity ratio and T_2^* intensity change ratio were determined using the following equations:

$$IR_t(\%) = \frac{I(long\ TE)_t}{I(short\ TE)_t} \times 100 \quad S(4)$$

$$\Delta IR\ (\%) = \frac{IR_{t=0}(long\ TE)}{IR_{t=i}(long\ TE)} \times 100 \quad S(5)$$

IR_t is a ratio of MRI signal intensities of images taken with long TE and short TE. $I(long\ TE)_t$ and $I(short\ TE)_t$ are corresponding ROI intensities at time points t, which were measured before contrast agent injection $t = 0$ and after injection $t = i$. ΔIR is MR image intensity changes resulting from binding of the contrast agent to the plaques, which was calculated from the ratios of image intensities acquired before ($IR_{t=0}$) and after ($IR_{t=i}$) contrast agent injection.

After the acquisition of MRI images, the animals were ethically euthanized. Their aortas were collected for fluorescence intensity evaluation, and other organs such as the liver, spleen, lung, kidney, and heart were harvested for histological investigations. Following this, the extracted organs and aortas were immersed in a 4% paraformaldehyde (PFA) solution in PBS for a day, then they were shifted to a PBS solution. The Azure Sapphire Biomolecular Imager was employed for capturing fluorescence images at an intensity setting of 1. The fluorescence intensity was

quantified utilizing ImageJ.

In vivo treatment test

ApoE$^{-/-}$ mice on a 7-week high-fat diet were separated into three groups, each comprising 6 mice, and were subjected to treatment for 4 weeks via tail vein injections twice a week. During each injection session, the mice were anesthetized using 2% isoflurane to ensure their comfort and minimize stress. Three days after the last injection, mice were humanely euthanized using cervical dislocation while under anesthetized with 2% isoflurane (Forane) administered via inhalation, ensuring minimal distress to the animals. Non-targeted mice received Chit-IOCO-Cy5, targeted mice were given Chit-IOCO-Cy5-MTX (1 mg /kg of MTX or 0.19 mg /kg of Cerium), and the control group was administered saline. Additionally, C57BL/6 mice were given saline to serve as a baseline control.

To evaluate plaque reduction and anti-inflammation, the mice's hearts and aortas were extracted. Liver, spleen, lung, and kidney were also harvested for histology studies. The aortas were divided into two parts for western blot studies and ORO staining (Scheme 2). The lower portions of the abdominal aortas were gathered to assess the inflammatory cytokines. These were then crushed on ice in 200 µL of lysis buffer for a period of 5 minutes (lysis buffer composition: 1% (V/V) Protease Inhibitor Cocktail, 1% Triton X-100, 20 mM Tris-HCl, 2.5 mM EDTA, 0.1% SDS, 1 mM $Na_4P_2O_7 \cdot 10\ H_2O$, 50 mM NaCl, 20 mM NaF, 1 mM Na_3VO_4, at pH 7.4). The remaining part of aortas was immersed in a 4% paraformaldehyde (PFA) solution for a day and was later replaced with a PBS solution.

Western blot analysis for samples from in vivo study

The homogenised aorta sections were subjected to centrifugation for 10 minutes at 4 °C. Subsequently, both the top fatty layer and the bottom fragments of the aorta were discarded, retaining only the middle protein solution layer for western blot analysis. Protein concentration was assessed via the microBCA assay kit. For each sample, approximately 30 µg of protein was mixed with 5× protein loading buffer, denatured (95°C for 5 mins), and introduced into a 12.5% SDS-PAGE gel. The proteins will be electrophoretically separated by initially running the SDS-PAGE gel at 80V for 15 minutes, followed by an increased voltage of 120V for an additional 50 minutes. These proteins were then transferred to a Mini LF PVDF membrane and subjected to triple wash cycles with 1× TBST (20 mM Tris, 150 mM NaCl, 0.1% (w/v) Tween® 20 detergent), each lasting 5 minutes. Subsequently, the membrane underwent blocking with 5% light milk in 1xTBST for 60 minutes and overnight incubation with primary antibodies targeting IL-6, TNF-α, COX-2, iNOS, or β-actin in a 4 °C with rocking. After incubation, the membranes were washed thrice with 1× TBST for 5 minutes and exposed to secondary anti-rabbit HRP antibodies at room temperature for an hour with rocking. Once each target protein's image was taken, the PVDF membranes were subjected to three cycles of treatment with stripping buffer (20mM Glycine, 1% SDS, in H_2O, pH 2.0 by HCl) for 10 minutes to remove any remaining antibodies on the membrane. The membranes were then re-blocked using the previously described

method. Chemiluminescent images of the LF PVDF membrane were captured with the Azure Sapphire Biomolecular Imager, and the gray values of chemiluminescence bands were measured using ImageJ.

ORO stain

Fat covering the aortas was removed, then the aortas were divided lengthwise and flattened. Aortas were washed 3 time with methanol followed by treated with oil red O. After 1h incubation, oil red O was removed and aortas were washed 3 time with methanol. The images were taken using KERN stereo zoom microscope OZL 464 with KERN microscope camera ODC832. The captured images were processed using ImageJ software, and the extent of the lesion was expressed as the area of the lesion-affected on the upper aortic surface.

Histology analysis

The collected organs went through a systematic processing procedure lasting for nine hours. This involved immersing them in ethanol of increasing concentrations (70%, 90%, 95%, and 100%), then treating them with xylene and paraffin. Following this, the samples were embedded in paraffin wax with the region of interest directed downwards. Sections of 4 μm thickness were then prepared using a Leica RM2235 paraffin microtome and arranged on designated SuperFrost Plus slides. These slides were stained with haematoxylin and eosin in a Tissue-Tek Prisma automatic stainer, and coverslips were affixed with the help of the attached Tissue-Tek-Glas automated cover slipper. Histological images were collected utilizing a microscope (CKX53, Olympus) with a digital camera (DP74, Olympus).

Statistical Analysis of Data

Data are presented as mean standard deviation. T-test, One-way ANOVA followed by Tukey's post-hoc analysis, and Two-way ANOVA followed by Šídák multiple comparisons test were used in the analysis of significant difference. For the preparation and characterization of the nanoparticles, three individual batches were synthesized and tested individually. Subsequently, the nanoparticles were scaled up for in vitro and in vivo experiments. For the in vitro experiments, the replicate numbers reported in the figure legends represent independent cell cultures. For the in vivo experiments, the replicate numbers correspond to the number of animals included in each experimental group. A p value of <0.05 was considered significant. Graphs were plotted using GraphPad Prism 8.

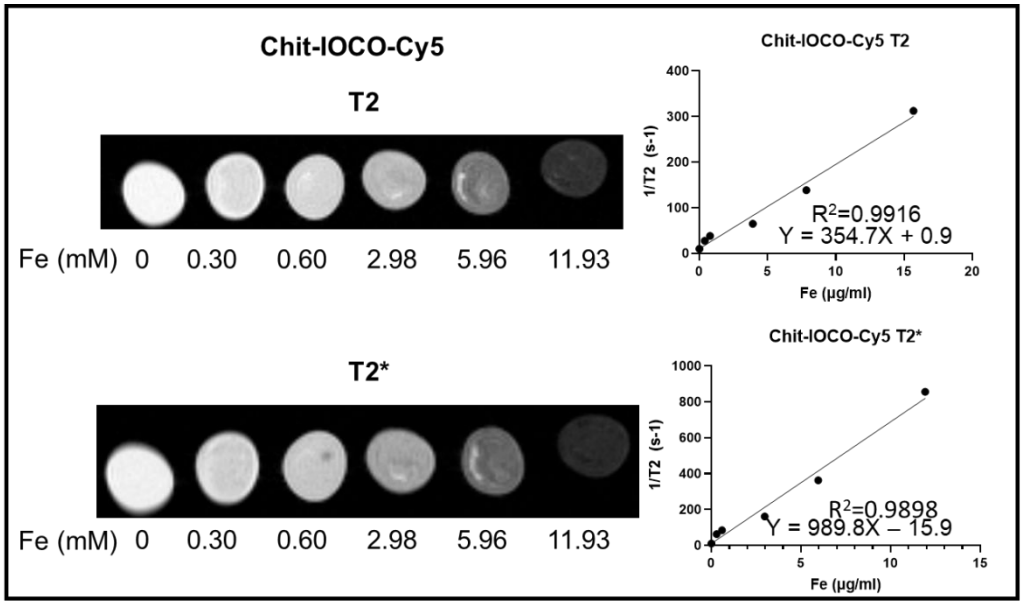

Figure S1. MRI of Chit-IOCO-Cy5 phantoms. The Nano-cocktails underwent dilution to different iron concentrations and then subjected to imaging via a 9.4 T MRI (i) MRI T2 and T2* images and the plotting of relaxation rate of Chit-IOCO-Cy5. T_2-weighted imaging: TE = 5 ms, TR = 2630 ms, T_2^*-weighted imaging: TE = 3 ms, TR = 300 ms. Bar = 1 mm

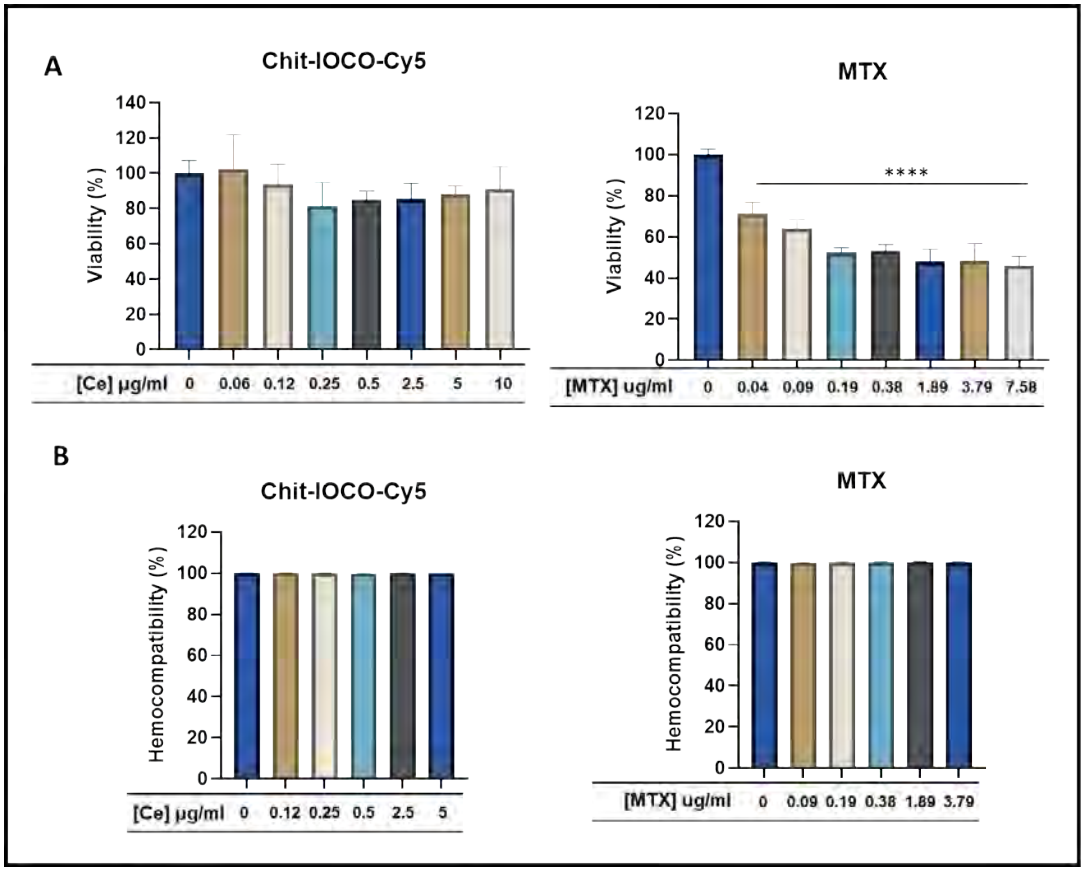

Figure S2. ***In vitro*** **biocompatibility of Chit-IOCO-Cy5 and free MTX. A)** Viability of RAW 264.7 cells treated with of Chit-IOCO-Cy5 or free methotrexate (MTX) at varying concentrations after 24-hour incubation. **B)** Haemocompatibility of Chit-IOCO-Cy5 and free MTX. Statistical significance was tested by one-way ANOVA followed by Tukey's post-hoc analysis. Mean ± S.D. **** $p < 0.0001$, ($n = 3$), compared to non-treated blood group.

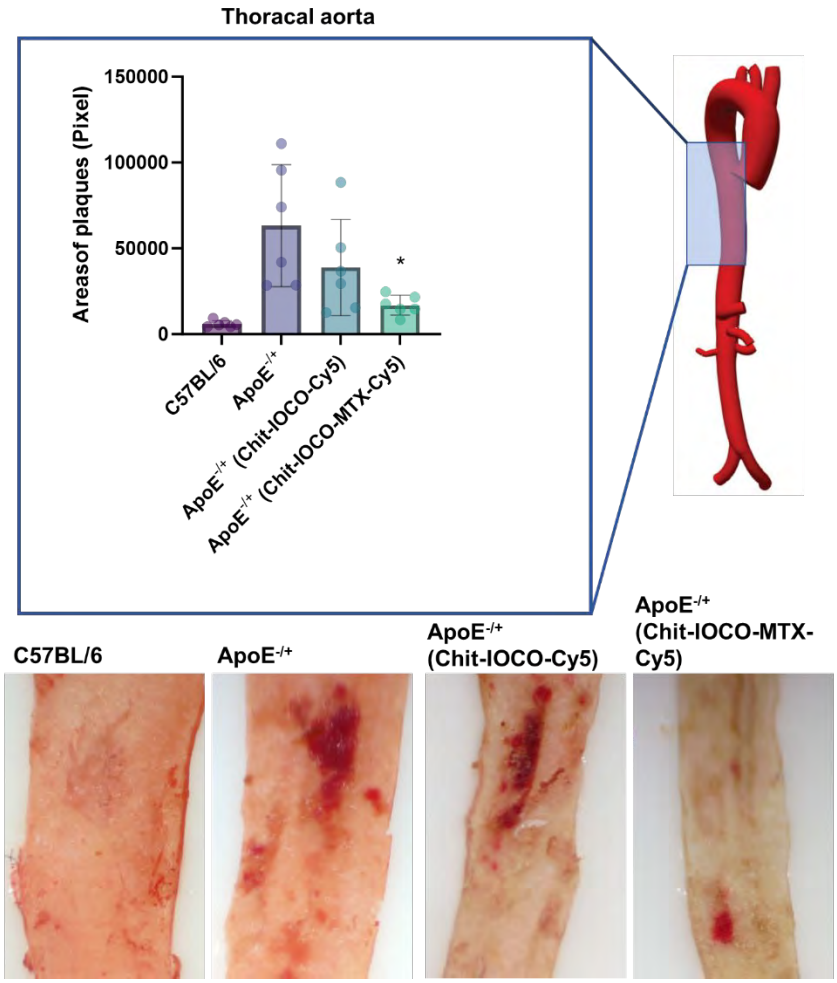

Figure S3. ORO staining of thoracal aorta. Quantification of the atherosclerotic plaque area for the thoracal aorta and the ORO staining images of the thoracal aorta in ApoE−/− mice that were administered Chit-IOCO-Cy5, Chit-IOCO-Cy5-MTX or saline for 4 weeks were analyzed. As a negative control, C57BL/6 mice were injected with saline for the same duration. Bar = 1 mm. Statistical significance was tested by one-way ANOVA followed by Tukey's post-hoc analysis. Mean ± S.D. *$p < 0.05$, ($n = 6$), compared to non-treated ApoE$^{-/-}$ mice.

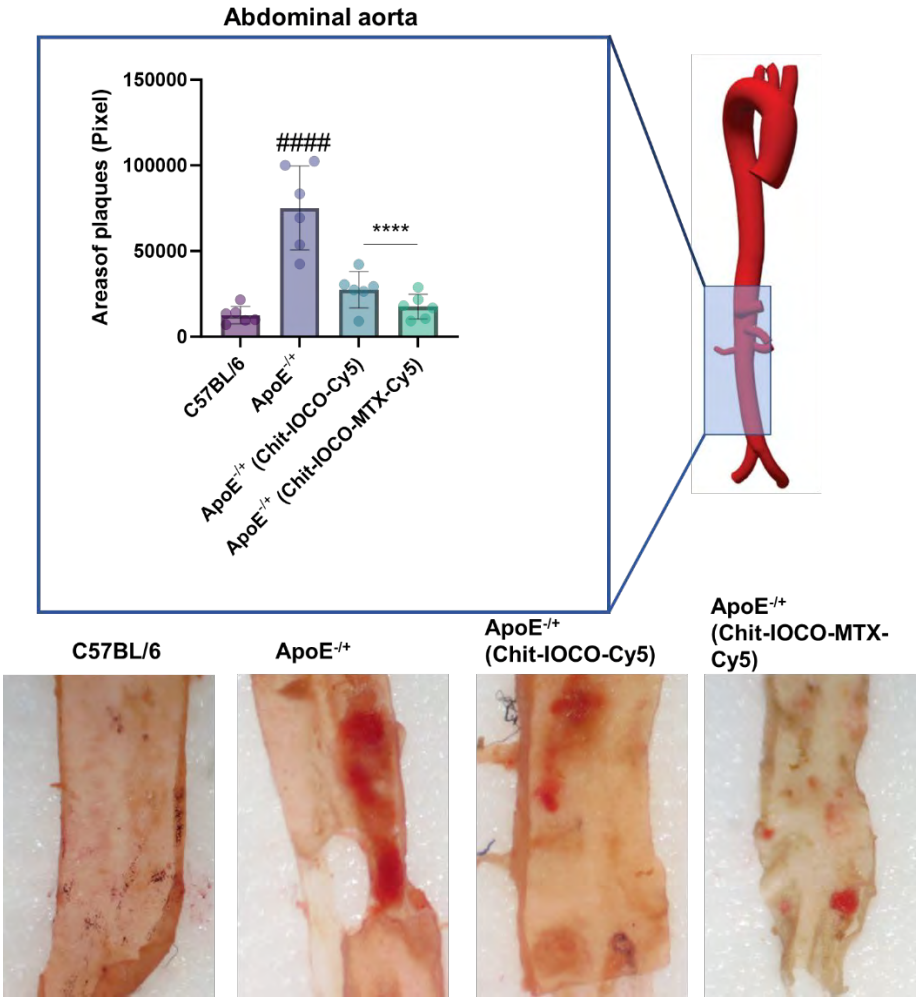

Figure S4. ORO staining of abdominal aorta. Quantification of the atherosclerotic plaque area for the abdominal aorta and the ORO staining images of the abdominal aorta in ApoE$^{-/-}$ mice that were administered Chit-IOCO-Cy5, Chit-IOCO-Cy5-MTX or saline for 4 weeks were analyzed. As a negative control, C57BL/6 mice were injected with saline for the same duration. Bar = 1 mm. Statistical significance was tested by one-way ANOVA followed by Tukey's post-hoc analysis. Mean ± S.D. **** $p < 0.0001$, (n = 6), compared to non-treated ApoE$^{-/-}$ mice.

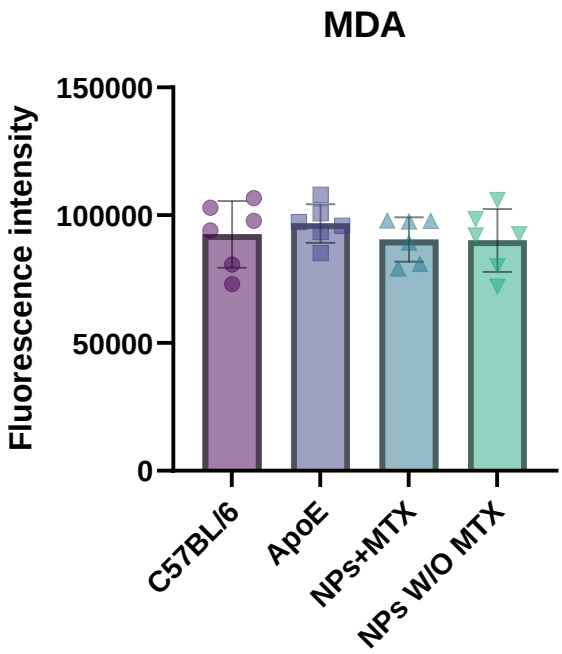

Figure S5. Serum malondialdehyde (MDA) level in ApoE$^{-/-}$ and wide type mice. Mice were administered with Chit-IOCO-Cy5, Chit-IOCO-Cy5-MTX or saline for 4 weeks were analyzed. n = 6

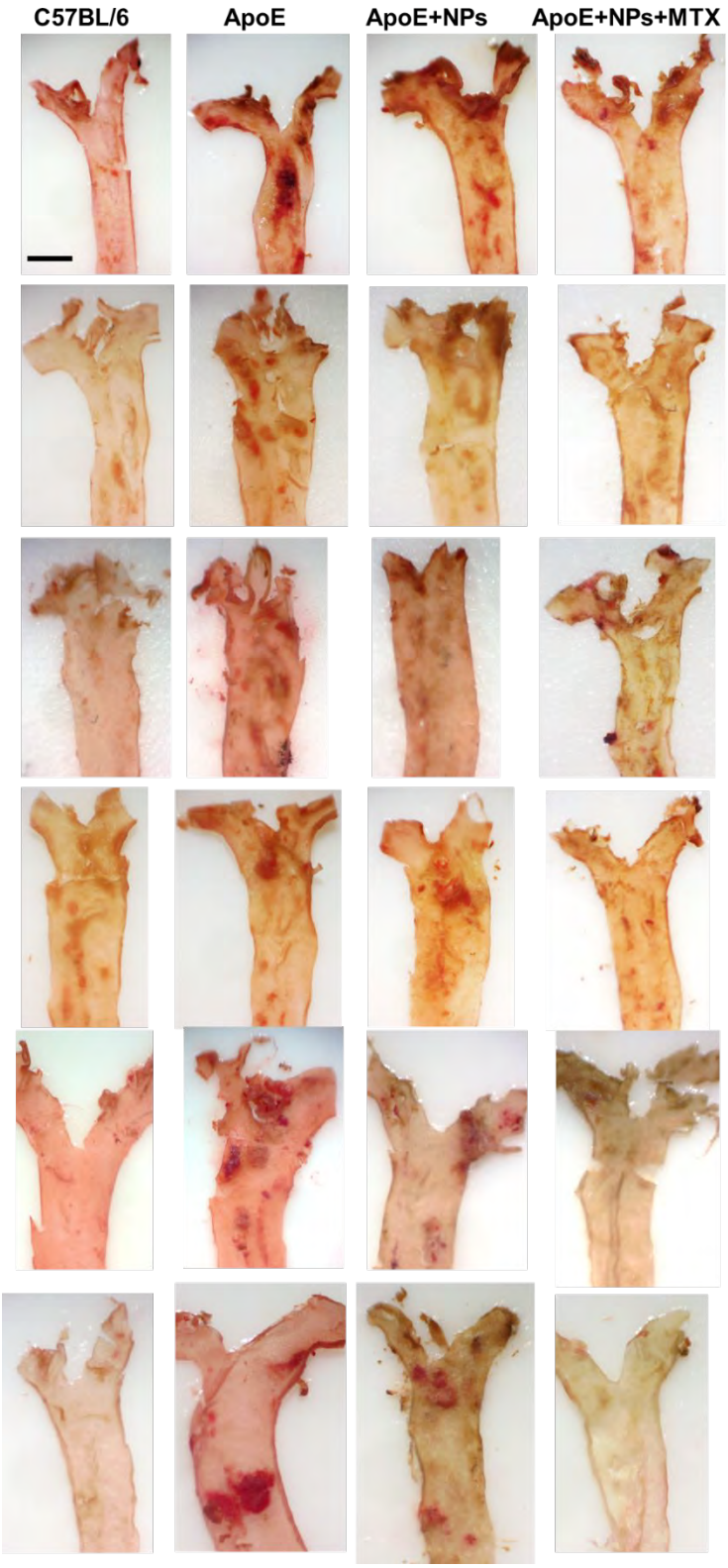

Figure S6. ORO staining of all aortic arches (upper panel) samples. The ORO staining images of the abdominal aorta in ApoE$^{-/-}$ mice that were administered Chit-IOCO-Cy5, Chit-IOCO-Cy5-MTX or saline for 4 weeks. n = 6, Bar = 1 mm.

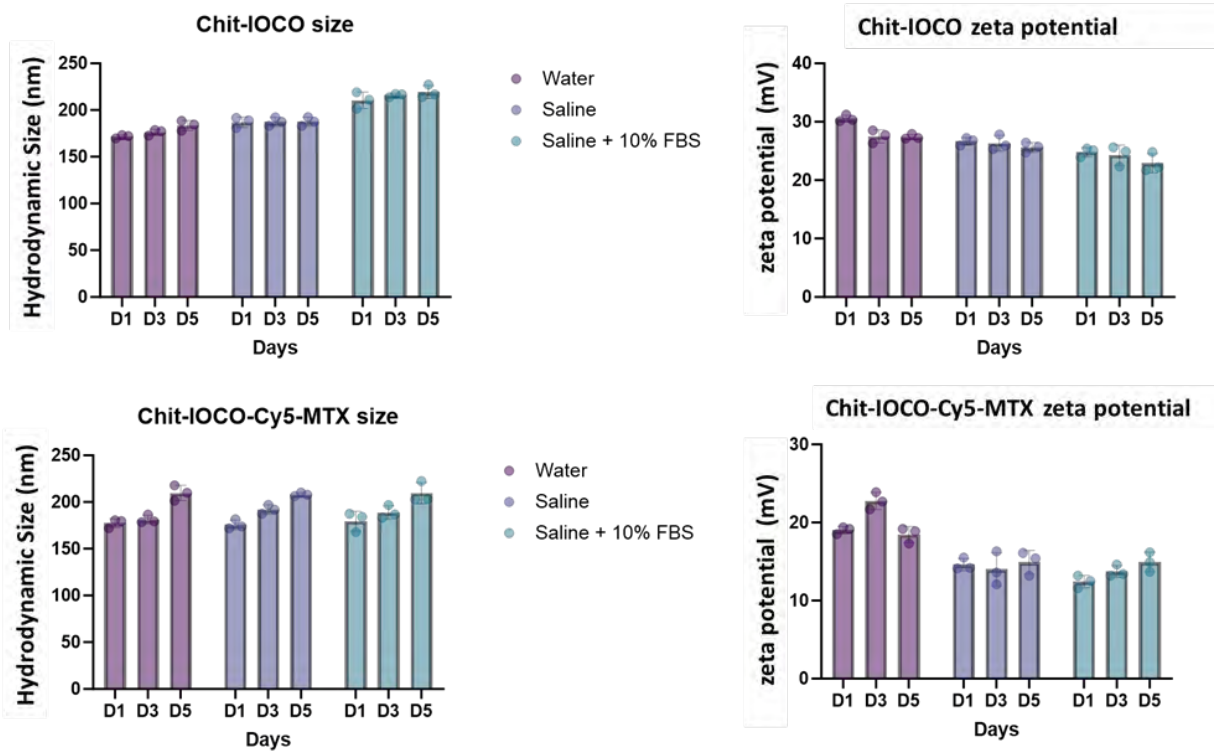

Figure S7. Stability study of the nanoparticles in the water, saline and saline with FBS. Size and zeta potential of Chit-IOCO-Cy5 and Chit-IOCO-Cy5-MTX added in water, saline and saline with 10% of FBS for 1, 3 and 5 days.

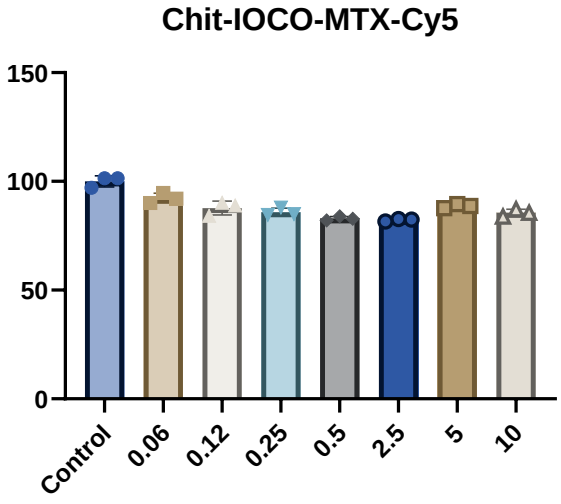

Figure S8. *In vitro* biocompatibility of Chit-IOCO-MTX-Cy5 A) Viability of CHO cells treated with of Chit-IOCO-MTX-Cy5 at varying concentrations after 24-hour incubation.

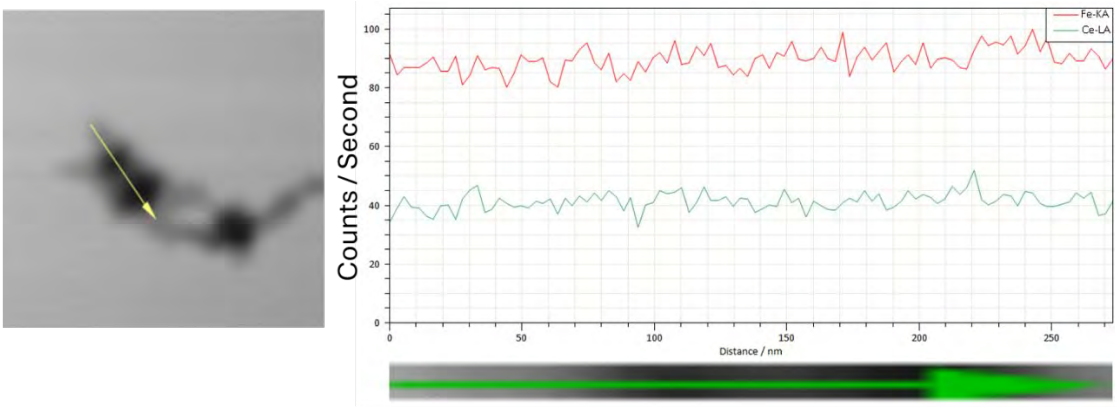

Element	Netto	Mass %	Atom%	Abs. error [%]	Abs. error [%]
Cerium	887	18.76	8.43	0.03	39.36
Iron	7597	81.24	91.57	0.03	10.90

Figure S9. The EDS analysis of Chit-IOCO-Cy5-MTX. Scanning transmission electron microscopy (STEM) image of a representative Chit-IOCO-Cy5-MTX nanoparticle with the corresponding energy-dispersive X-ray spectroscopy (EDS) line scan analysis. The yellow arrow indicates the line along which elemental distribution was measured. The EDS line profiles of Fe-Kα (red) and Ce-Lα (green) show stable intensities along the scanned distance, confirming the homogeneous distribution of iron oxide and cerium oxide within the nanoparticle.

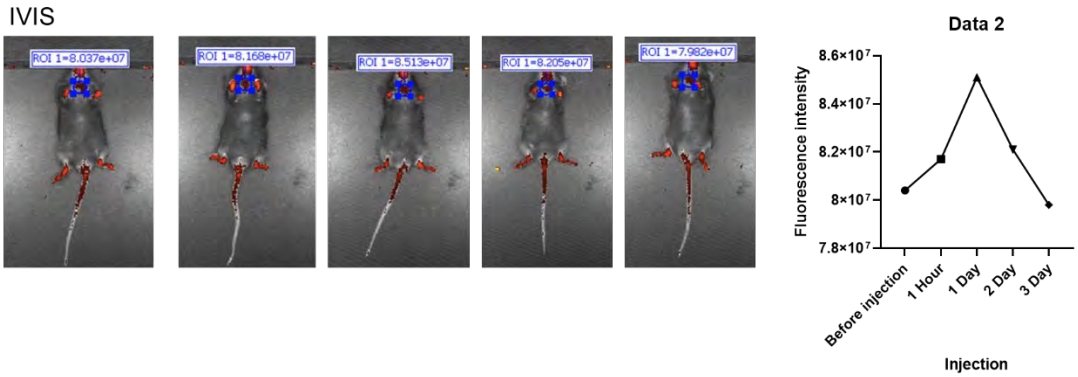

Figure S10. Optimization of imaging time points using in vivo fluorescence imaging (IVIS). Representative IVIS fluorescence images of ApoE−/− mice at different time intervals (1 h, 1 day, 2 days, and 3 days) following intravenous injection of Chit-IOCO-Cy5-MTX nanoparticles. Quantification of fluorescence intensity within the atherosclerotic region (region of interest, ROI) indicated that the signal peaked at 24 h post-injection.

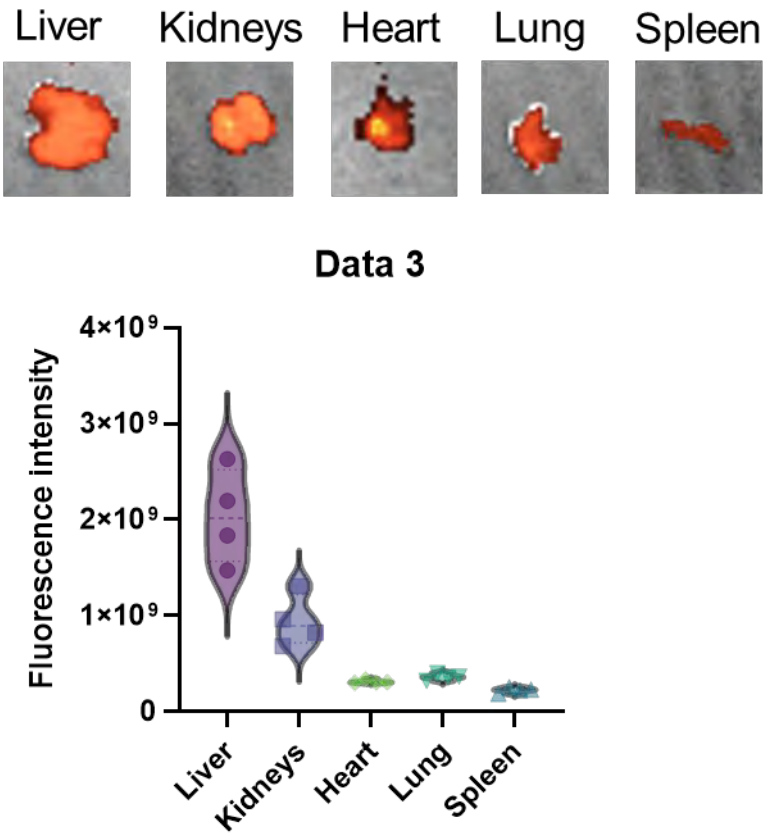

Figure S11. Ex vivo biodistribution of Chit-IOCO-Cy5-MTX nanoparticles in major organs. Representative ex vivo fluorescence images of harvested organs (liver, spleen, kidney, lung, and heart) at 48 h post-intravenous injection of Chit-IOCO-Cy5-MTX nanoparticles. Quantitative analysis of fluorescence intensity (bottom panel) demonstrates predominant accumulation of the nanoparticles in the liver and kidneys, consistent with expected nanoparticle clearance pathways. (n = 4).

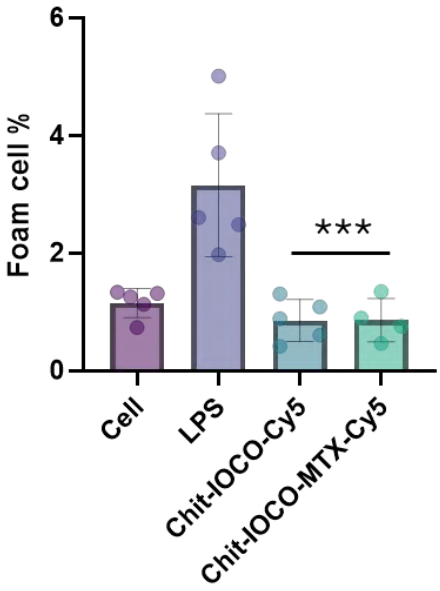

Figure S12. Chit-IOCO-Cy5 and Chit-IOCO-Cy5-MTX reduce foam cell formation in LPS-stimulated macrophages. Quantification of foam cells in RAW 264.7 macrophages treated with LPS (1 μg/mL) with or without Chit-IOCO or Chit-IOCO-Cy5-MTX (0.25 μg/mL Ce). Foam cells were assessed by Oil Red O staining, expressed as percentage of total cells. Data represent mean ± SD (n = 4-5). *** $P<0.001$.

References

1. Wu, Y.; Zhang, R.; Tran, H. D. N.; Kurniawan, N. D.; Moonshi, S. S.; Whittaker, A. K.; Ta, H. T., Chitosan Nanococktails Containing Both Ceria and Superparamagnetic Iron Oxide Nanoparticles for Reactive Oxygen Species-Related Theranostics. *ACS Applied Nano Materials* **2021,** *4* (4), 3604-3618.

2. Wu, Y.; Zhang, R.; Tran, H. D.; Kurniawan, N. D.; Moonshi, S. S.; Whittaker, A. K.; Ta, H. T., Chitosan nanococktails containing both ceria and superparamagnetic iron oxide nanoparticles for reactive oxygen species-related theranostics. *ACS Applied Nano Materials* **2021,** *4* (4), 3604-3618.